UNCLASSIFIED

# AN INVESTIGATION OF AN APPROACH TO THE PROBLEM OF DETERMINING THE OPTIMUM DESIGN OF SHROUDED PROPELLERS

APPENDIX I. VORTEX SYSTEM

APPENDIX II. CALCULATION OF THRUST AND POWER

APPENDIX III. DETERMINATION OF THE OPTIMUM LOADING FOR A HEAVILY LOADED PROPELLER HAVING AN INFINITE NUMBER OF BLADES

By

Robin B. Gray

APPENDIX IV. OUTLINE OF DESIGN PROCEDURES FOR SHROUDED PROPELLERS

By

Walter Castles, Jr., and Robin B. Gray

Daniel Guggenheim School of Aeronautics

Project No. 9R 38-01-017-24

Contract No. DA-44-177-TC-402
Job Order No. 2

U. S. Army Transportation Research Command
Fort Eustis, Virginia



May, 1960

REC 60-44

Engineering Experiment Station
Georgia Institute of Technology
Atlanta, Georgia

AN INVESTIGATION OF AN APPROACH TO THE PROBLEM

OF DETERMINING THE OPTIMUM DESIGN OF SHROUDED PROPELLERS

Prepared by: Robin B. Gray

Robin B. Gray, Associate Professor
Daniel Guggenheim School of Aeronautics

Approved by: Thomas W. Jackson

Thomas W. Jackson, Chief
Mechanical Sciences Division

Released by: J. E. Boyd

James E. Boyd, Director
Engineering Experiment Station

The findings and recommendations contained in this report are those of the contractor and do not necessarily reflect the views of the Chief of Transportation.

UNCLASSIFIED

Engineering Experiment Station
Georgia Institute of Technology
Atlanta, Georgia

# AN INVESTIGATION OF AN APPROACH TO THE PROBLEM OF DETERMINING THE OPTIMUM DESIGN OF SHROUDED PROPELLERS

APPENDIX I. VORTEX SYSTEM

APPENDIX II. CALCULATION OF THRUST AND POWER

APPENDIX III. DETERMINATION OF THE OPTIMUM LOADING FOR A HEAVILY LOADED PROPELLER HAVING AN INFINITE NUMBER OF BLADES

By

Robin B. Gray

APPENDIX IV. OUTLINE OF DESIGN PROCEDURES FOR SHROUDED PROPELLERS

By

Walter Castles, Jr., and Robin B. Gray

Daniel Guggenheim School of Aeronautics

Project No. 9R 38-01-017-24

Contract No. DA-44-177-TC-402
Job Order No. 2

U. S. Army Transportation Research Command
Fort Eustis, Virginia

May, 1960

TREC 60-44

TABLE OF CONTENTS


| | Page |
|---|---|
| SUMMARY | 1 |
| INTRODUCTION | 2 |
| NOTATION | 4 |
| POTENTIAL TANK METHOD | 9 |
| DIGITAL COMPUTER METHOD | 24 |
| DISCUSSION | 36 |
| CONCLUSIONS AND RECOMMENDATIONS | 39 |

APPENDICES

| | |
|---|---|
| APPENDIX I - VORTEX SYSTEM | I-1 |
| APPENDIX II - CALCULATION OF THRUST AND POWER | II-1 |
| APPENDIX III - DETERMINATION OF THE OPTIMUM LOADING FOR A HEAVILY LOADED PROPELLER HAVING AN INFINITE NUMBER OF BLADES | III-1 |
| APPENDIX IV - OUTLINE OF DESIGN PROCEDURES FOR SHROUDED PROPELLERS | IV-1 |
| REFERENCES | IV-12 |

## FIGURES IN TEXT


| Figure | | Page |
|---|---|---|
| 1. | Die and drawing apparatus | 11 |
| 2. | Die used in helix forming operation | 13 |
| 3. | Cellulose acetate helix used in construction of two-bladed wake model | 14 |
| 4. | Electrical potential model of the ultimate wake of an optimum, lightly-loaded, two-bladed shrouded propeller | 15 |
| 5. | Electrical potential model of the ultimate wake of an optimum, lightly-loaded, four-bladed shrouded propeller | 17 |
| 6. | Details of electrical potential model of the ultimate wake of an optimum, lightly-loaded, two-bladed shrouded propeller | 18 |
| 7. | Details of probe | 18 |
| 8. | Probe mounted on traverse mechanism | 19 |
| 9. | Schematic wiring diagram | 20 |
| 10. | Variation of nondimensional optimum blade bound vortex strength distribution function with nondimensional blade radial station for two shrouded propellers as determined from potential measurements and a comparison with a theoretical distribution for a shrouded propeller having an infinite number blades | 22 |
| 11. | Coordinate systems | 26 |
| 12. | Comparison of two methods of computing the variation in nondimensional optimum blade bound vortex distribution with blade station for free propellers | 34 |


## FIGURES IN APPENDICES


| Figure | | |
|---|---|---|
| I-1 | Velocity diagram in the ultimate wake | I-2 |
| I-2 | Cross-section of wake vortex system of a two-bladed single-rotation propeller in the vicinity of the shroud trailing edge. Shroud is removed from the flow for illustrative purposes | I-5 |

FIGURE IN APPENDICES (continued)


| Figure | | Page |
|---|---|---|
| I-3 | Vortex system on shroud mean camber surface showing non-rotating components of shroud bound vortex distribution and the continuation of the blade tip bound vortex into the shroud contour with its subsequent spreading out and shedding at the shroud trailing edge as the wake boundary vortex system | I-7 |
| I-4 | Cross-section of the vortex system of a two-bladed, single-rotation, shrouded propeller as visualized for the analyses of this report | I-9 |
| II-1 | Control volume used in determining the thrust | II-1 |
| II-2 | Wake vortex system showing the various paths along which the line integrals are calculated | II-4 |
| II-3 | Paths along which line integrals must be evaluated to show that the line integral about a path enclosing the wake is zero | II-7 |
| II-4 | Region adjacent to intersection of inner helical sheet with boundary sheet | II-9 |
| II-5 | Path of integration within wake | II-13 |
| III-1 | Velocity diagram for outermost filament of inner vortex sheet and the adjacent boundary filament | III-2 |
| III-2 | Relationship of boundary filaments to inner helical sheet filaments | III-3 |
| IV-1 | Vortex pattern used in shroud design | IV-5 |
| IV-2 | Location of vortex rings for determination of outer shroud contour | IV-8 |

## SUMMARY

Two methods of obtaining the necessary optimum combination of design parameters for a lightly loaded, single rotation shrouded propeller are described for the case in which the ultimate wake vortex pattern moves as a rigid body and is composed of helical vortex filaments of equal geometric pitch. One method employs the electrical potential tank techniques while the other uses a digital computer to numerically integrate the Biot-Savart relation. The use of both methods to determine the optimum blade bound vortex distribution for a two-bladed shrouded propeller whose ultimate wake helical vortex filaments have a geometric pitch of 1.356 and the assumed geometric configuration was investigated. In addition, the distribution for a four-bladed shrouded propeller, having the same wake geometric pitch, was determined by the potential tank method. An outline of the use of the data so obtained in designing an optimum propeller is presented.

The theoretical analysis of a heavily loaded shrouded or free propeller having an infinite number of blades is given in an appendix.

## INTRODUCTION

It was established in Reference 1 by A. Betz that the optimum free propeller (i.e. an isolated propeller having the highest possible kinetic or induced efficiency) is characterized by an ultimate wake vortex system whose motion through the fluid medium is as if the wake vortex sheets formed a rigid screwlike structure of uniform pitch. It is possible to determine the necessary radial distribution of the wake vortex sheet strength for such a system and this has been done, initially for the lightly loaded two and four-bladed propeller by S. Goldstein in Reference 2, and later for propellers having various numbers of blades and for the range of wake helix angles of interest by T. Theodorsen in Reference 3.

In considering the comparable ultimate wake vortex system for the optimum, lightly loaded, shrouded propeller, the same arguments and considerations hold as to the pitch and movement of the vortex sheet that is shed from the blade trailing edge; that is, the pitch of the vortex sheet must be constant and the sheet must appear to move as a rigid structure. However, there is an additional boundary condition which requires that the flow at the trailing edge of the shroud be tangent to the shroud mean camber surface at this point or in other words, the Kutta condition for the shroud trailing edge must be satisfied. For this to occur, a sheet of vorticity must be shed from the shroud trailing edge. If it is assumed that the shroud is "long enough" for the wake to have reached its ultimate configuration at the shroud trailing edge, then this boundary vortex sheet consists of helical vortex filaments wrapped on a right circular cylinder. Thus, for the lightly loaded case, the vortex filaments in the outer boundary sheet and in the inner helical sheet have the same geometric pitch and satisfy the necessary conditions imposed. The geometry of this ultimate wake vortex system is discussed in greater detail in Appendix I.

Once the geometry of the wake vortex system has been thus defined, the determination of the vortex strengths becomes a relatively straightforward process. Two such methods will be discussed in this report. The

first is modeled after the potential tank techniques developed by T. Theodorsen in Reference 3. The second is a numerical evaluation of the Biot-Savart integral by means of a digital computer.

The potential tank approach is based on the well-known analogue between the velocity potential of a perfect fluid flow and the electrical potential of a uniformly conducting medium. For the case under consideration, the differential velocity-potential-equation for the flow field associated with the vortex sheets is identical, after a change in variable, with the differential electrical-potential-equation for the field in the potential tank that is associated with sheets of insulating material of the same geometry as the vortex sheets. An exposition of the potential tank techniques in presented in Reference 4. The determination of the necessary propeller parameters thus can be determined from the measurement of the corresponding electrical potential in the conducting medium with the transformed boundary conditions.

The approach using the classical vortex theory is also well-established. In this instance, the vortex sheets are approximated by a number of finite strength vortex filaments. The Biot-Savart integral is then numerically integrated for the velocity components induced by each filament at each calculating point with the strength of the filament being initially unspecified. The vortex filament strengths are then determined by a simultaneous solution of the resulting equations using the necessary restraints and boundary conditions.

A discussion of each of these approaches follows.

## NOTATION

| | |
|---|---|
| $A_n$ | element of area under curve of shroud bound vortex distribution versus distance along shroud |
| $b$ | number of blades |
| $c$ | blade chord |
| $c_d$ | blade airfoil sectional profile drag coefficient |
| $C_{D_S}$ | shroud drag coefficient based on wake cross-sectional area |
| $c_l$ | blade airfoil sectional lift coefficient |
| $c_p$ | power coefficient based on wake cross-sectional area, $c_s + e$ |
| $c_{p_d}$ | increment to power coefficient due to profile drag |
| $c_{p_T}$ | total power coefficient, $c_p + c_{p_d}$ |
| $c_s$ | thrust coefficient based on wake cross-sectional area, $\frac{T}{\frac{1}{2}\rho V_\infty^2 F}$ |
| $c_{s_d}$ | increment to thrust coefficient due to profile drag |
| $c_{s_T}$ | net thrust coefficient, $c_s - c_{s_d}$ |
| $e$ | induced energy loss coefficient based on wake cross-sectional area, $\frac{E}{\frac{1}{2}\rho V_\infty^2 F V_\infty}$ |
| $E$ | induced energy loss per unit time in the wake |
| $F$ | ultimate wake cross-sectional area |
| $H$ | geometric pitch of ultimate wake helix |
| $k$ | shroud bound vortex proportionality constant |
| $K(x)$ | circulation function for single rotation, $\frac{b\Gamma\Omega}{2\pi(V_\infty + w)w}$ |
| $L$ | axial distance between successive vortex sheets, $\frac{H}{b}$ |
| $L'$ | lift per unit span, $\rho V \Gamma$ |
| $M$ | number of vortex filaments used in approximating wake vortex system |

| | |
|---|---|
| $p$ | local static pressure |
| $p'$ | static pressure in disturbed fluid with respect to fixed co-ordinates |
| $p_\infty$ | static pressure in free stream |
| $\Delta Q$ | increment in torque due to addition or removal of vortex element $\Delta\Gamma$ |
| $r$ | blade radial station or radial location of calculating point |
| $r'$ | radius of vortex filament |
| $R$ | propeller radius |
| $R_o$ | ultimate wake radius |
| $ds'$ | element of length of vortex filament |
| $dS$ | element of area of control surface |
| $dS'$ | element of area of vortex sheet surface |
| $t$ | time |
| $T$ | thrust |
| $\Delta T$ | element of thrust due to addition or removal of vortex element $\Delta\Gamma$ |
| $v_w$ | unit sink strength |
| $x$ | non-dimensional blade station or location of calculating point, $\frac{r}{R}$ ; $\frac{r}{R_o}$ |
| $x'$ | non-dimensional radius of vortex filament |
| $z_o'$ | axial location of vortex filament |
| $\beta$ | angle defined in the Biot-Savart relation |
| $\gamma$ | unit strength of assumed wake boundary vortex sheet |
| $\Gamma(r)$ | blade bound vortex distribution or function of $r$ |
| $\Gamma(\zeta)$ | wake boundary vortex sheet strength |
| $\Gamma_m$ | strength of $n^{\underline{th}}$ shroud bound vortex ring |
| $\Delta\Gamma$ | element of bound vorticity added or removed |

| | |
|---|---|
| $\epsilon$ | axial loss factor |
| $\eta$ | efficiency net thrust to power input ratio |
| $\eta_i$ | ideal efficiency |
| $\theta$ | control surface co-ordinate |
| $\varkappa$ | strength of vortex filament |
| $\varkappa$ | mass coefficient or total induced velocity loss factor |
| $\lambda$ | tangent of helix angle of outermost radial vortex filament in the ultimate wake, $\tan \varphi_o$ |
| $\rho$ | density of incompressible fluid medium |
| $P$ | distance from vortex element ds' to calculating point |
| $\sigma$ | blade solidity, $\frac{bc}{2\pi r}$ |
| $\varphi$ | pitch angle of vortex sheet |
| $\varphi'$ | pitch angle of vortex filament |
| $\varphi_o$ | pitch angle of outermost radial vortex filament in the ultimate wake |
| $\phi$ | total velocity potential |
| $\phi'$ | induced velocity potential |
| $\psi$ | azimuth location of blade bound vortex or calculating point |
| $\psi'$ | azimuth location of vortex element ds' |
| $\Psi_s$ | stream function associated with shroud bound vortex system |
| $\Psi_s^*$ | non-dimensional stream function associated with vortex ring |
| $\Psi_{s_{T.E.}(r',z')}$ | stream function at shroud trailing edge due to a shroud bound vortex ring |
| $\Psi_T$ | total volume of flow or total stream function |
| $\Psi_{T.E.}$ | total stream function or total volume flow required through shroud trailing disk area |
| $\Psi_{V_\infty}$ | stream function associated with the free stream velocity |

$\Psi_w$ stream function associated with the assumed uniform cylindrical wake vortex sheet

$\Psi_w^*$ non-dimensional stream function associated with the uniform sink strength distribution

Co-ordinate Systems

$x, y, z$ Cartesian co-ordinate system fixed in space

$x'_m, y'_m, z'_m$ Cartesian co-ordinate system fixed in vortex pattern. $x, y, z$ and $x'_m, y'_m, z'_m$ are considered to be coincident for the analysis

$r, \psi, z$ Cylindrical co-ordinate system corresponding to $x'_m, y'_m, z'_m$ space

$r, \xi, \zeta$ helical co-ordinate system (Figure 11)

Velocities

$u_x, u_y, u_z$ induced velocity components parallel to $x, y, z$ axes respectively

$\Delta u_{x_m}, \Delta u_{y_m}, \Delta u_{z_m}$ increments in induced velocity associated with $m^{\text{th}}$ vortex filament

$u_r, u_\xi, u_\zeta$ induced velocity components parallel to helical co-ordinates $r, \xi, \zeta$

$u_{\xi_o}$ induced velocity at and parallel to the wake axis

$\bar{u}_{\xi_o}$ $u_{\xi_o} / V_\infty$

$u_\psi$ tangential induced velocity component

$v$ total induced velocity

$v_z$ time average axial component of velocity in ultimate wake

$V$ total velocity

$V_i$ induced velocity

$V_\infty$ free stream velocity or propeller-shroud velocity along flight path

| | |
|---|---|
| $w_p$ | induced axial inflow velocity at propeller plane |
| $w$ | parameter describing the apparent axial motion of the wake vortex system |
| $\bar{w}$ | $w/V$ |
| $w_R$ | parameter describing the apparent axial motion of the wake boundary vortex system |
| $\Omega$ | angular velocity of the blades |

Subscripts

| | |
|---|---|
| m | denotes particular vortex filament |
| R | denotes quantity at wake boundary |
| $R_o^-$ | denotes quantity just inside wake boundary |
| $R_o^+$ | denotes quantity just outside of wake boundary |
| p | denotes quantity at propeller blade axis or plane |

## POTENTIAL TANK METHOD

### Apparatus

The geometry of the models was determined from the analysis given in Appendix I. Thus, the wake vortex system was considered to be composed of an inner helical sheet of vortex filaments of constant geometric pitch and an outer sheet of helical vortex filaments of constant pitch wrapped on a right circular cylinder, the pitch of the outer filaments being equal to that of the outermost filament of the inner helical sheet. The electrical potential analogue of this system was obtained by constructing a physical model of the vortex pattern from an insulating material. Then the analogue of the outer cylindrical sheet is simply an insulated right circular cylinder and the analogue of the inner sheet is a helical sheet of constant geometric pitch formed from an insulating material. In this particular case, the model also becomes the potential tank by the addition of conducting end plates mounted at right angles to the axis of the cylinder.

A commercially available acrylic tube, six inches in diameter and about 53 inches long with a one-eighth inch wall was used for the outer cylinder. The inner helical sheet was formed from 0.02-inch thick cellulose acetate sheet which is also available commercially. A description of the method of forming the plastic helices follows.

Several different combinations of heating baths, dies, materials, sheet thicknesses, and forming methods were investigated or tried with varying degrees of success. During the early attempts, the plastic material was completely immersed in a quenching-type oil bath which was heated electrically and maintained at a constant temperature by thermostat controls. Several simple forming dies were tried. The first one was a simple slot cut in one-eighth inch thick aluminum sheet. This die was mounted at the surface of the heated oil and the plastic sheet of the proper width was pulled through the die with a twisting motion. The results of this operation were so poor that this method was immediately

discontinued. The next apparatus consisted of two one-eighth inch diameter steel rollers mounted above the oil bath, one set being displaced spirally from the other set to yield the desired helix angle. Very good results were obtained at the edges of the helix, but the center of the helix was excessively wrinkled when the sheet was pulled through the rollers with a twisting motion. Some time was spent in experimenting with oil bath temperature, air blast cooling, and pre-loading the rollers, but these wrinkles could not be eliminated. For the next step, a die was constructed having a spiral slot of the proper pitch and width. When the sheet was pulled through this die, a satisfactory helix was obtained for about one-quarter to one-half turn, but the plastic sheet would then buckle and the remainder of the sheet was unusable. Additional supports were provided by rollers and the plastic was cooled by the vapor from liquid carbon dioxide. Different sheet thicknesses and materials were tried as follows: in cellulose acetate, 0.02", 0.03", 0.04", 0.06"; in cellulose acetate butyrate, 0.015"; and in cast acrylic, one-sixteenth inch sheet which was the thinest available locally. Of these, the 0.02" thick cellulose acetate yielded the best results so that further efforts were restricted to this material and thickness.

Additional experimentation showed that better results were obtained if the plastic sheet was not soaked in the heated oil bath for an appreciable length of time. Consequently, the drum of hot oil was replaced by a shallow pan of heated oil through which the plastic sheet was pulled just prior to its entering the die. During this experimental phase, a silicone release agent was added to the quenching oil in a one part release agent to about sixteen parts of oil by volume, which seemed to aid the forming operation. It was subsequently discovered that the roller supports, the cooling, and the forced twisting motion which was mechanically imparted to the sheet were unnecessary. A photograph of the forming apparatus in its final configuration is presented as Figure 1.

The drawing mechanism consisted of a fully swiveling clamp mounted on a carriage which ran on and was positioned by a set of vertical tracks. The motive power was provided by a hand operated winch not shown in the photograph.

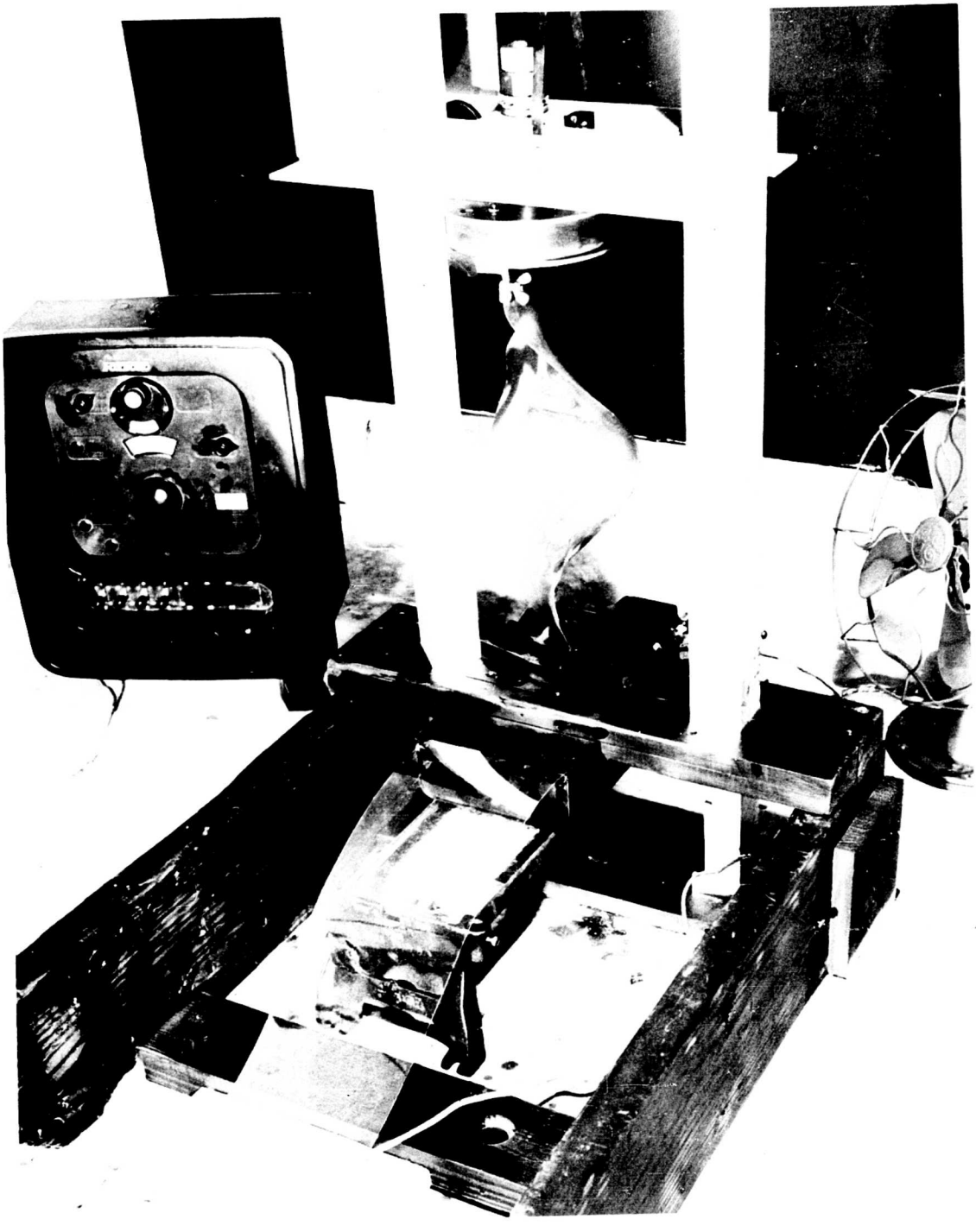

Figure 1. Die and Drawing Apparatus.

The die is shown in Figure 2. It was constructed of wood and each half was mounted on a wooden base plate. The one and one-half inch thick base plates when clamped together also acted as guides to the plastic sheet. A one and three-eighths inch diameter wooded roller was mounted on the underside of one base plate to act not only as a guide but to insure that the plastic sheet was completely immersed in the oil. The dimensions of the die did not appear to be critical. In this case, the die was constructed from a piece of Honduras mahogany one and one-eighth inches thick and had a geometric pitch of about three-fifths the desired geometric pitch.

The forming operation as described below resulted in about one usable helix for every three tries. The oil bath was maintained at 315°F $\pm$ 2°F. A sheet of clear cellulose acetate 5.75 inches by eight feet long by 0.02 inches thick was clamped to the swivel on the carriage. The carriage was lowered to the die surface and a fold of the plastic sheet was immersed in the hot oil. When the sheet had become soft, the carriage was raised and the die was clamped shut about the softened portion. The carriage was then steadily raised at about two to three inches per minute thereby drawing the plastic sheet through the die. It was found that, when conditions were right, an almost perfect helix was obtained. The helix used in the construction of the two-bladed model is shown in Figure 3.

The construction of the two-bladed model was relatively simple. The helical sheet was inserted into the six-inch diameter acrylic tube and a bead of glue was laid along the contact lines. This model is shown in Figure 4.

The construction of the four-bladed model proved to be much more difficult. Two helices of the same geometric pitch were chosen and one of these was cut along its centerline. These two half helices were cemented one to a side of the second helix along its centerline thereby forming two helical sheets which intersected at right angles. This part of the construction was successfully completed. However, when the helices were inserted into the 53-inch long acrylic tube, it was found that slight inaccuracies in joining the two sheets resulted in unacceptable deformations in the helices when inserted in the tube. For this

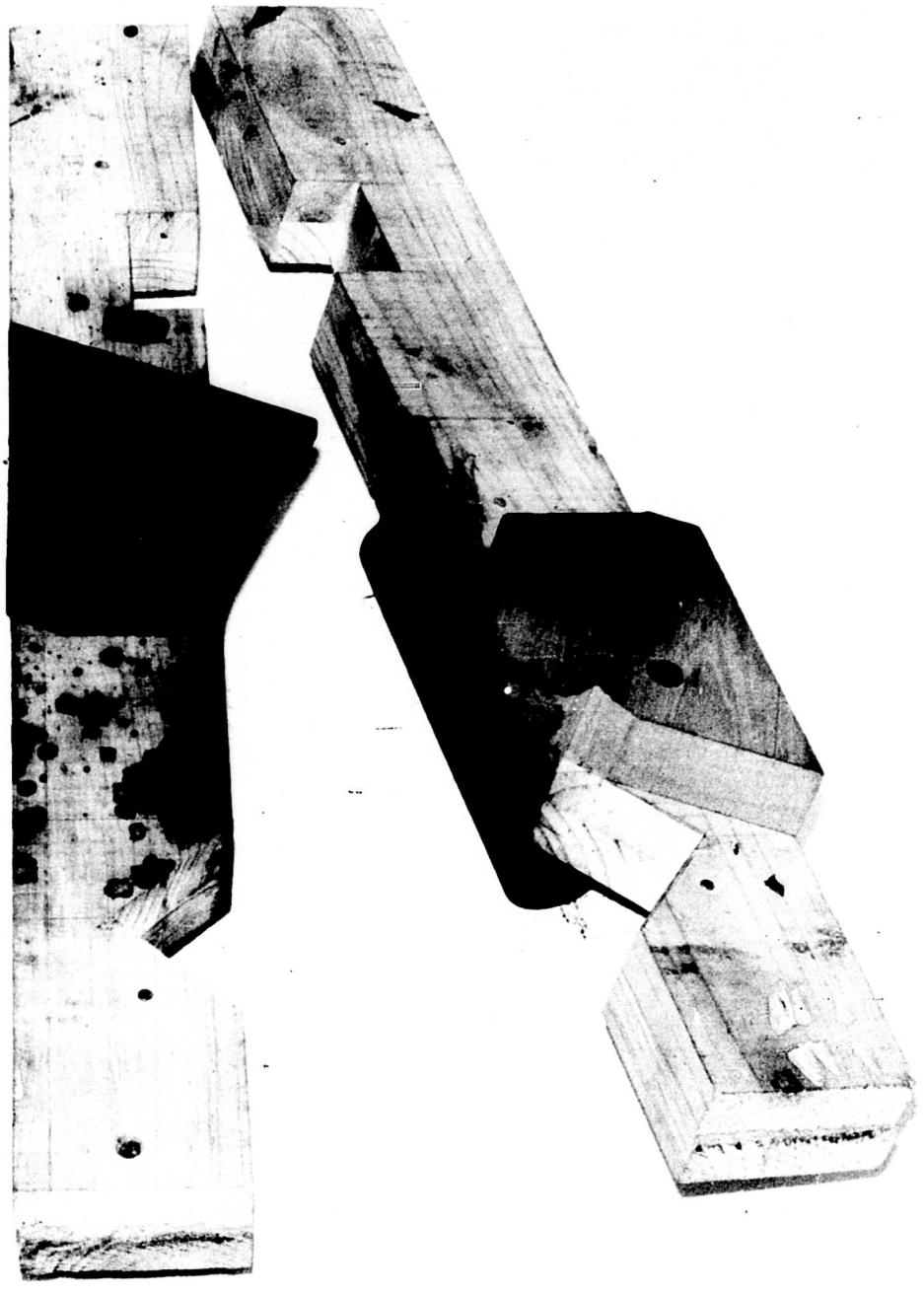

Figure 2. Die Used in Helix Forming Operation.

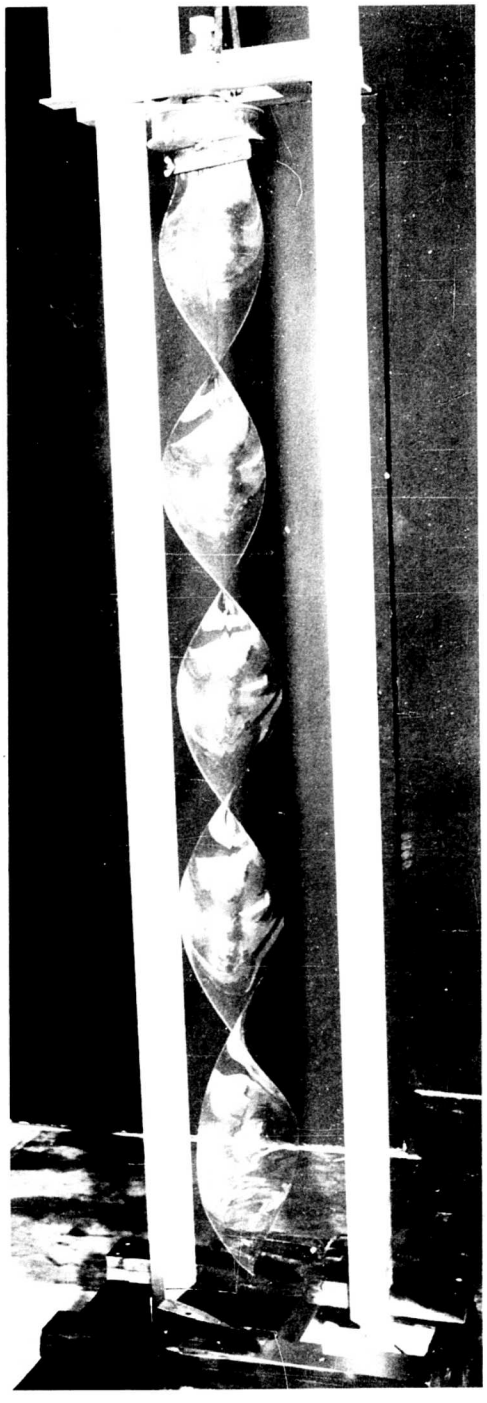

Figure 3. Cellulose Acetate Helix Used in Construction of Two-Bladed Wake Model.

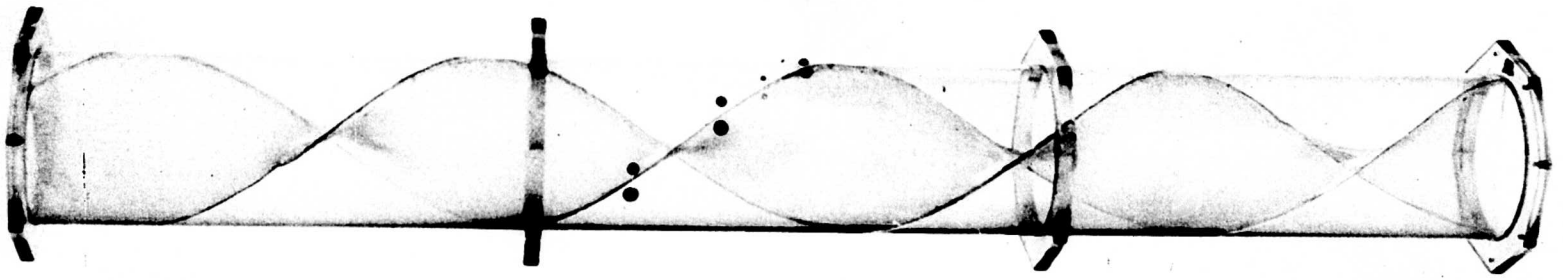

Figure 4. Electrical Potential Model of the Ultimate Wake of an Optimum, Lightly-Loaded, Two-Bladed Shrouded Propeller.

reason and in view of the results that had been obtained on the two-bladed model, it was decided to simplify the design of this model and to construct only one of the spiral flutes. In the construction, a spiral quarter section was cut from the acrylic tube. One of the helical sheets was cut along its axis, glued together again along this same axis but so as to form a right angle, and then the resulting form was cemented to the inside of the remaining three-quarter section of the tube thus forming one of the spiral flutes of the four-bladed propeller wake model. This resulted in a much more accurate model than could have been obtained in the original construction as all of the glue lines were readily accesible for gluing and clamping in place. The potential tank model of the four-bladed propeller wake is shown in Figure 5.

For a reason to be given later, a two-foot section of tube was added to either end of the wake models when the measurements were made. The electrodes were placed at the ends of these additions. A sketch of the resulting potential tank apparatus is given in Figure 6.

The probe with which the measurements were taken was constructed of 0.1-inch glass tubing with a 0.010-inch diameter platinum wire conductor. Details of the probe are shown in Figures 7 & 8. The potential readings were obtained in decibels from a standing wave indicator.

The power supply was a 400-cycle aircraft generator driven by a synchronous motor through a timing-belt drive. A schematic wiring diagram of the electrical system is given in Figure 9.

Experimental Procedures

After the model construction was completed, the models were checked for leaks by running a small amount of mineral spirits along the glue lines. When the leaks so determined had been stopped, one end of the two-bladed model was sealed, the model was filled with tap water, and the resistance between the two sides was determined by running a wire probe simultaneously down each side of a glue line. At all points, the measurement was of the order of $10^7$ ohms, so it was assumed that the electrical leakage would be negligible. Since there was only one flute in the four-bladed model this latter test was not necessary.

The measurements were first made on the two-bladed wake model. The two end tubes containing the electrodes were connected to the wake

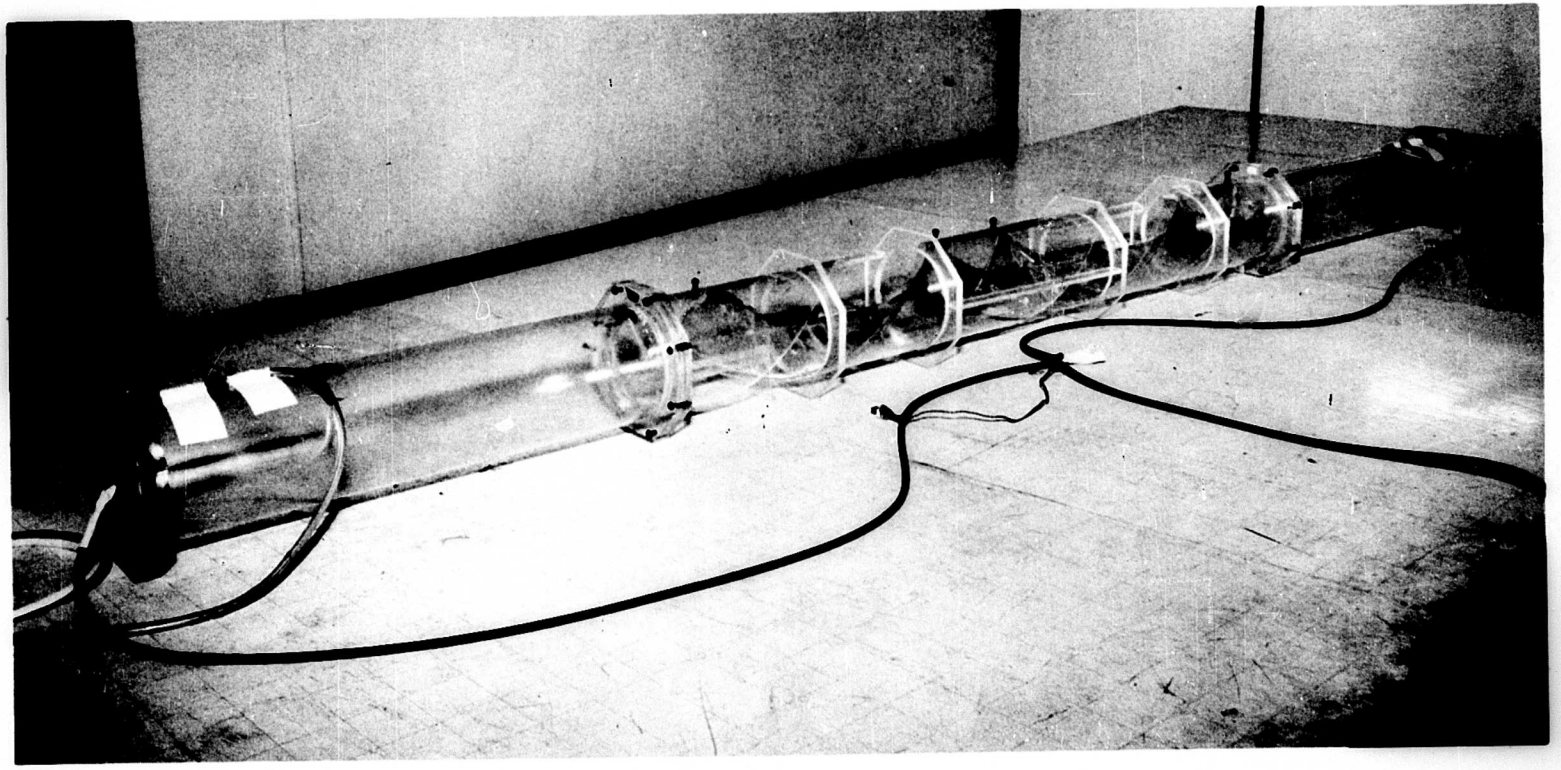

Figure 5. Electrical Potential Model of the Ultimate Wake of an Optimum, Lightly-Loaded, Four-Bladed Shrouded Propeller.

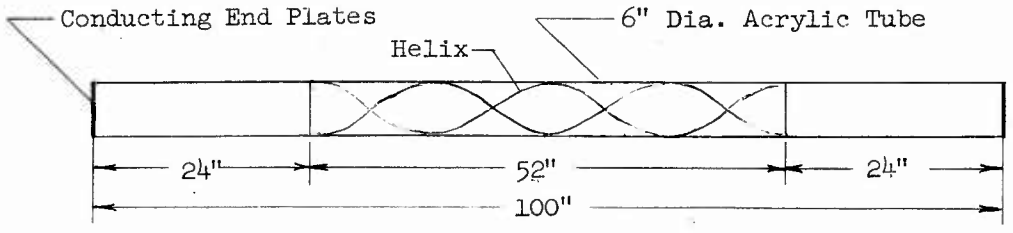


Figure 6. Details of electrical potential model of the ultimate wake of an optimum, lightly-loaded, two-bladed shrouded propeller.

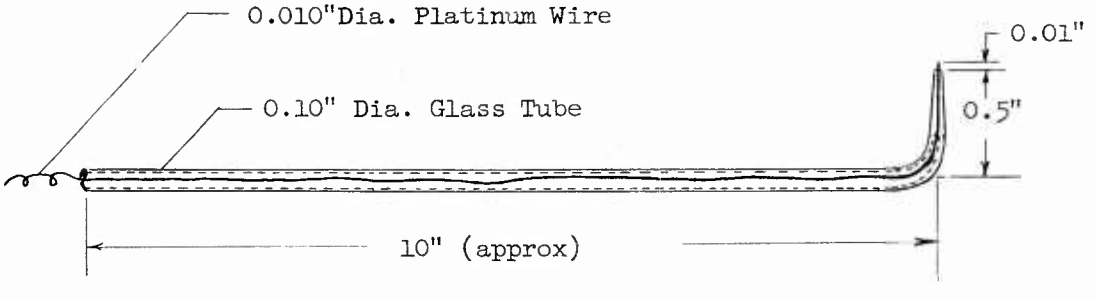


Figure 7. Details of probe.

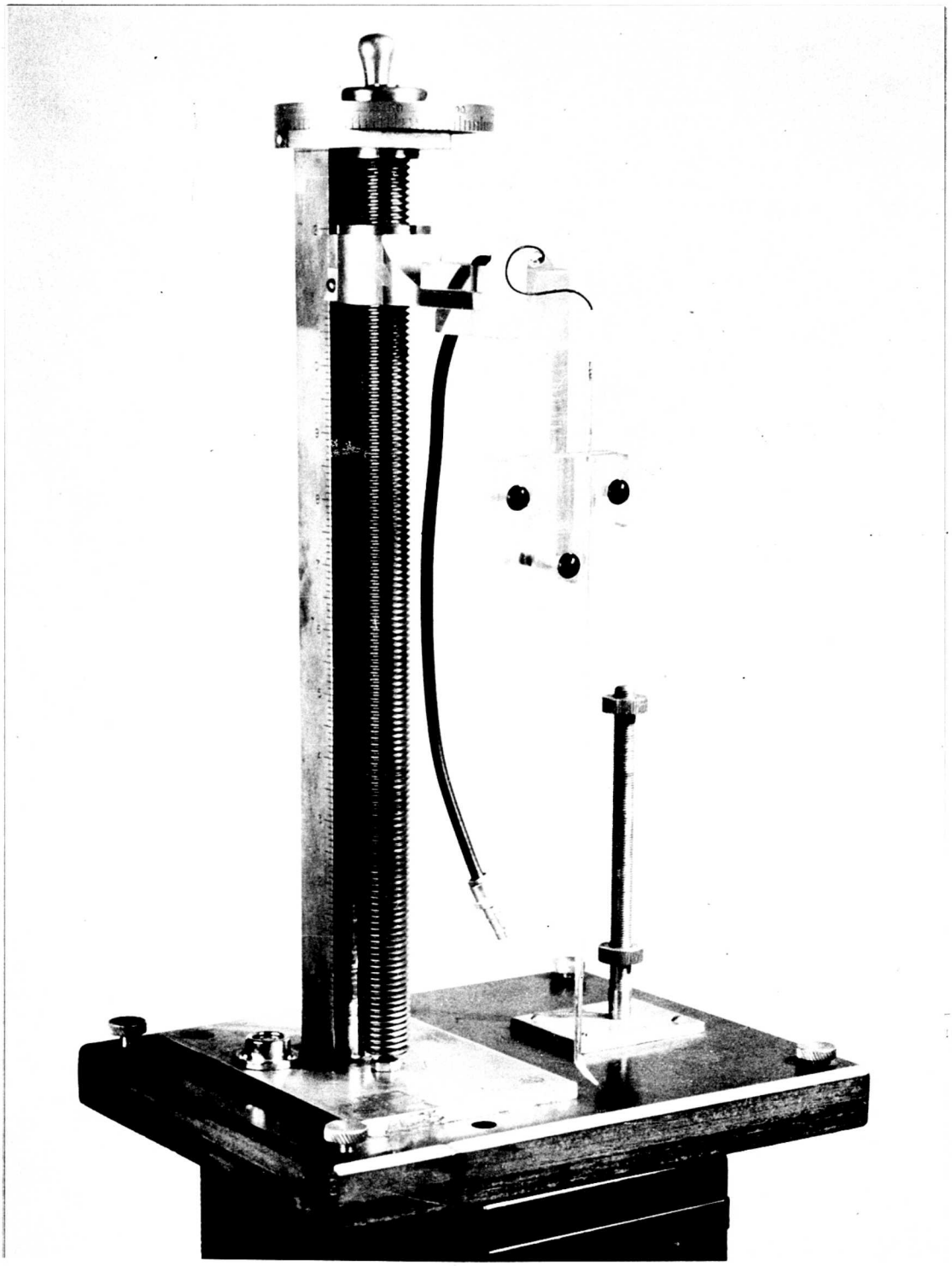

Figure 8. Probe Mounted on Traverse Mechanism.

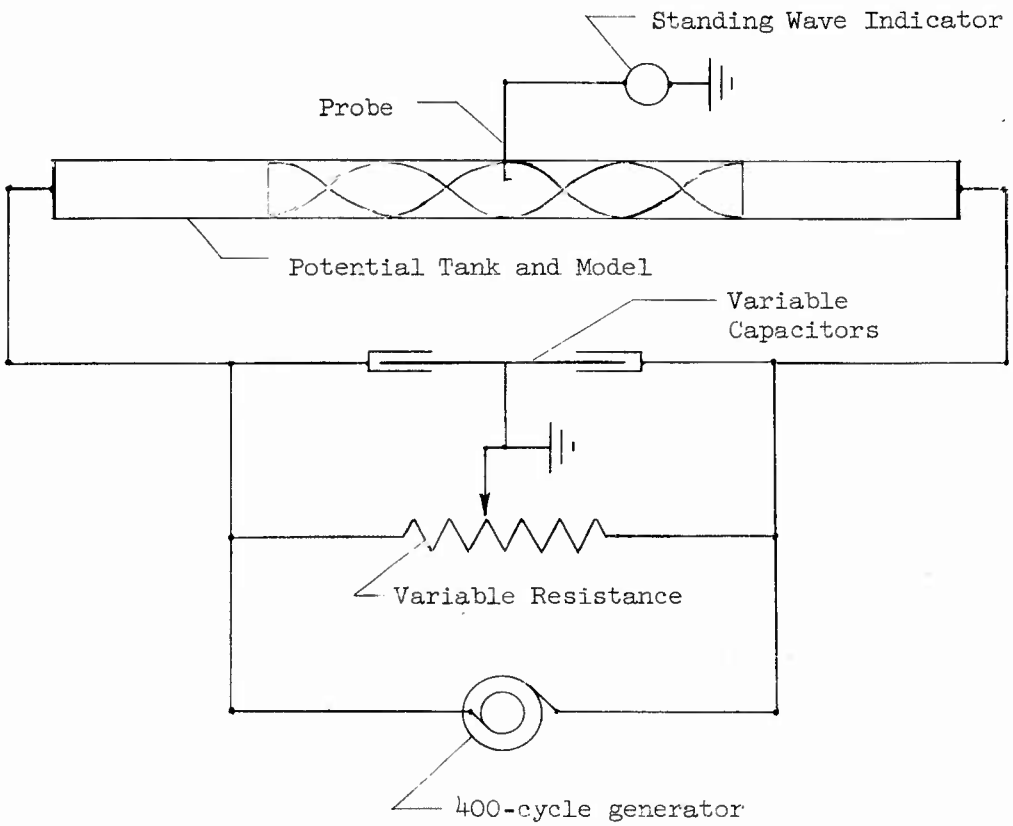


Figure 9. Schematic wiring diagram.

model and the resulting configuration was very slowly filled with tap water which had been standing in closed containers for a period of about 24 hours to allow as much of the dissolved air as possible to escape. When the model was completely filled, it was placed in a horizontal position. The 400-cycle power supply was then started and a 135-volt potential was applied across the model. The probe was introduced into the fluid at the model midpoint through a hole in the model wall and was so positioned that the exposed platinum wire was on the surface of the helical plastic sheet at the axis of the model. The capacitive and resistive bridges were adjusted until the meter on the standing wave indicator indicated a minimum voltage reading. A vertical traverse was made across the helical sheet and the voltage readings at the sheet surface were recorded. The voltage variation along the axis of the model at the sheet surface was also determined and recorded. The probe was then placed at the model axis on the other side of the sheet and the traverses were repeated. In order to investigate the effects of the ends, the model was rotated one-sixteenth turn and the measurements were recorded for this position, which was closer to one end. This procedure was repeated several times at each traverse station.

Essentially the same techniques were used for the four-bladed wake model, except that the traverses could only be made across a radius.

Experimental Results

The non-dimensional results, along with the theoretical distribution for an infinite number of blades, are presented in Figure 10 and correspond to the K(x) function of Theodorsen in Reference 3. This is the non-dimensional blade bound vortex distribution as defined by the following relation:

$$K(x) = \frac{b \Omega \Gamma(r)}{2\pi (V_\infty + w) w} \qquad (1)$$

where $b$ the number of blades
$r$ radial co-ordinate
$R$ blade radius
$\Gamma(r)$ the blade bound vortex strength at radius $r$

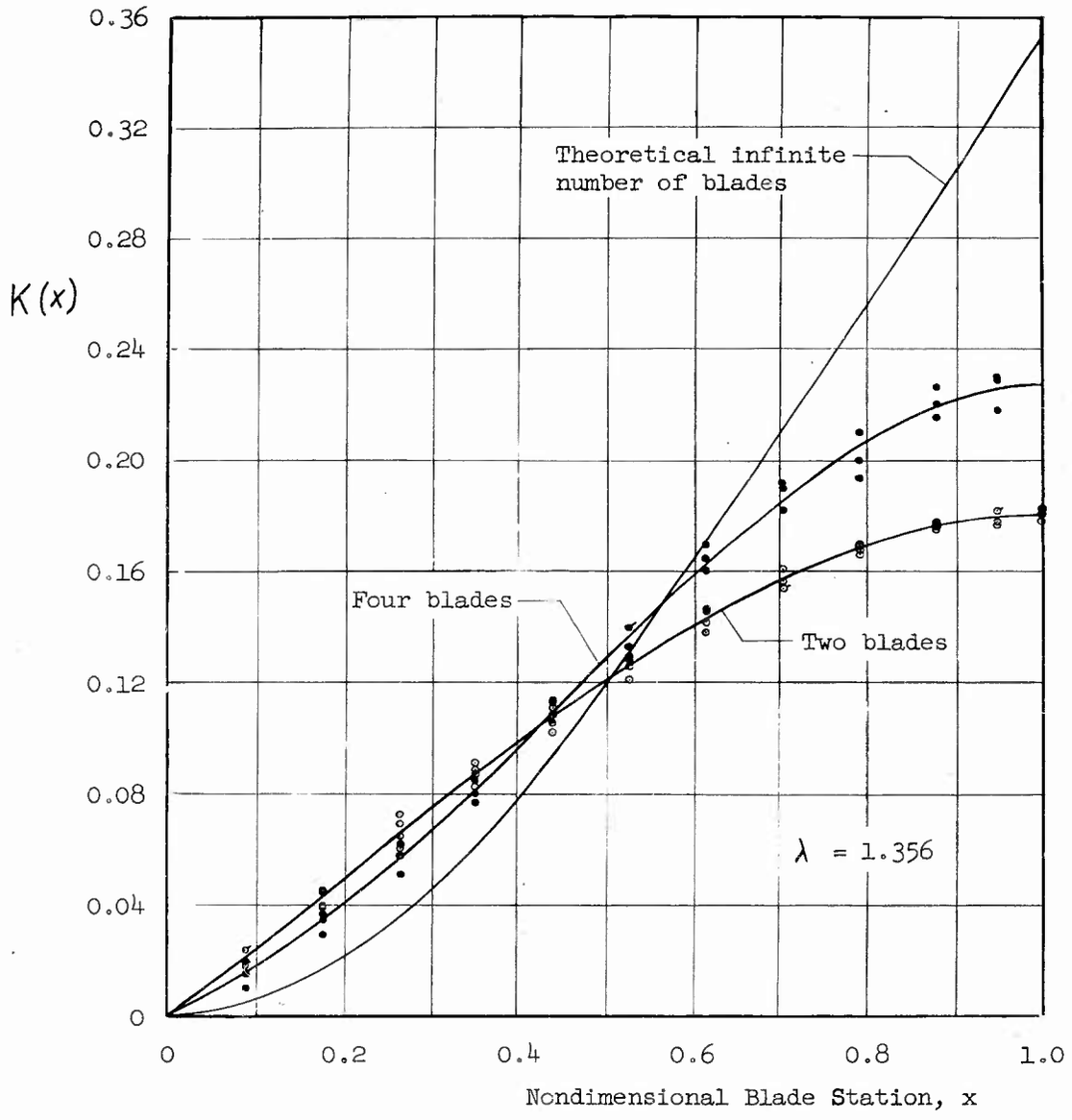


Figure 10. Variation of nondimensional optimum blade bound vortex strength distribution function with nondimensional blade radial station for two shrouded propellers as determined from potential measurements and a comparison with a theoretical distribution for a shrouded propeller having an infinite number blades. Plotted points are representative and not inclusive.

$\Omega$ the angular velocity of the blades

$V_\infty$ free stream velocity

$w$ parameter describing the apparent axial motion of the wake vortex system

$x$ non-dimensional radial station, $r/R$

This $K(x)$ distribution was obtained from the potential models by dividing the potential drop across the sheet by the potential drop between successive sheets.

It is estimated that experimental error is about $\pm$ 2 per cent of the maximum readings. The maximum difference between readings taken at the same radial station, but at different axial stations, was about $\pm$ 5 per cent of the maximum readings and is a measure of the geometric accuracy of the model. The curves presented in Figure 10 represent the average values of several radial surveys taken at several different axial stations. Plotted points are representative only and not inclusive.

The values of the mass coefficient or total induced velocity loss parameter $\varkappa$ for the three cases was determined from the definition

$$\varkappa = 2\int_0^1 K(x)\, x\, dx$$

For the two-bladed propeller, $\varkappa = 0.141$; for the four-bladed propeller, $\varkappa = 0.165$; and for the infinite number of blades, $\varkappa = 0.200$. These correspond to the free propeller values of 0.059, 0.096, and 0.200, respectively.

## DIGITAL COMPUTER METHOD

### Theoretical Analysis

The methods of classical vortex theory are well-established so that only those changes which pertain to this particular problem will be presented. In this case, a vortex system of known geometry and motion (i.e. right circular helical sheet of infinite length which appears to move as a solid body) is given, and the problem is to find the distribution of vorticity which will satisfy these given boundary conditions. The Biot-Savart equation supplies the necessary relation between the geometry, the motion, and the vortex sheet strength. It may be written as follows:

$$dV_\lambda = \frac{\varkappa}{4\pi} \frac{\cos\beta \, ds'}{P^2} \qquad (2)$$

where $dV_i$ increment in velocity that is associated with a vortex sheet element of length $ds'$ and width $dr$ at a point

$\varkappa$ strength of vortex filament

$\beta$ angle between normal to element $ds'$ and displacement vector, $\bar{P}$ from $ds'$ to the point; measured in the plane determined by $d\bar{s}'$ and $P$

$ds'$ length of elemental vortex filament

$P$ distance from element $ds'$ to the point under consideration

The integral relations for the velocity components in Cartesian co-ordinates are given in Reference 5, page 211, and are repeated below for the vortex sheet system which has been replaced by M finite strength vortex filaments.

$$\Delta u_{x_m} = \frac{\varkappa_m}{4\pi} \int \left\{ \frac{dy'}{ds'} \frac{z-z'}{P} - \frac{dz'}{ds'} \frac{y-y'}{P} \right\}_m \frac{ds'}{P_m^2} \qquad (3a)$$

$$\Delta u_{y_m} = \frac{\kappa_m}{4\pi}\int\left\{\frac{dz'}{ds'}\,\frac{x-x'}{P} - \frac{dx'}{ds'}\,\frac{z-z'}{P}\right\}_m \frac{ds'}{P_m^2} \qquad (3b)$$

$$\Delta u_{z_m} = \frac{\kappa_m}{4\pi}\int\left\{\frac{dx'}{ds'}\,\frac{y-y'}{P} - \frac{dy'}{ds'}\,\frac{x-x'}{P}\right\}_m \frac{ds'}{P_m^2} \qquad (3c)$$

where $x, y, z$ Cartesian co-ordinates defining the point P. The z-axis and the axis of the vortex system coincide with the positive z-direction in the direction of advance of the vortex system

$x'_m, y'_m, z'_m$ Cartesian co-ordinates defining the position of the vortex sheet element ds' of the $m^{\underline{th}}$ filament

$\Delta u_{x_m}, \Delta u_{y_m}, \Delta u_{z_m}$ velocity components parallel to the x-, y-, and z-axes respectively associated with the $m^{\underline{th}}$ vortex filament.

$$P_m = \left\{(x-x'_m)^2 + (y-y'_m)^2 + (z-z'_m)^2\right\}^{\frac{1}{2}} \qquad (4)$$

The components are more conveniently expressed in polar co-ordinates so that the following co-ordinate transformation is made. See Figure 11.

$$\left.\begin{aligned} x'_m &= r'_m \cos\psi'_m \\ x &= r\cos\psi \\ y'_m &= r'_m \sin\psi'_m \\ y &= r\sin\psi \\ z'_m &= z'_{0_m} + r'_m\psi'_m \tan\varphi'_m \\ z &= z \\ s'_m &= r'_m\psi'_m \sec\varphi'_m \end{aligned}\right\} \qquad (5)$$

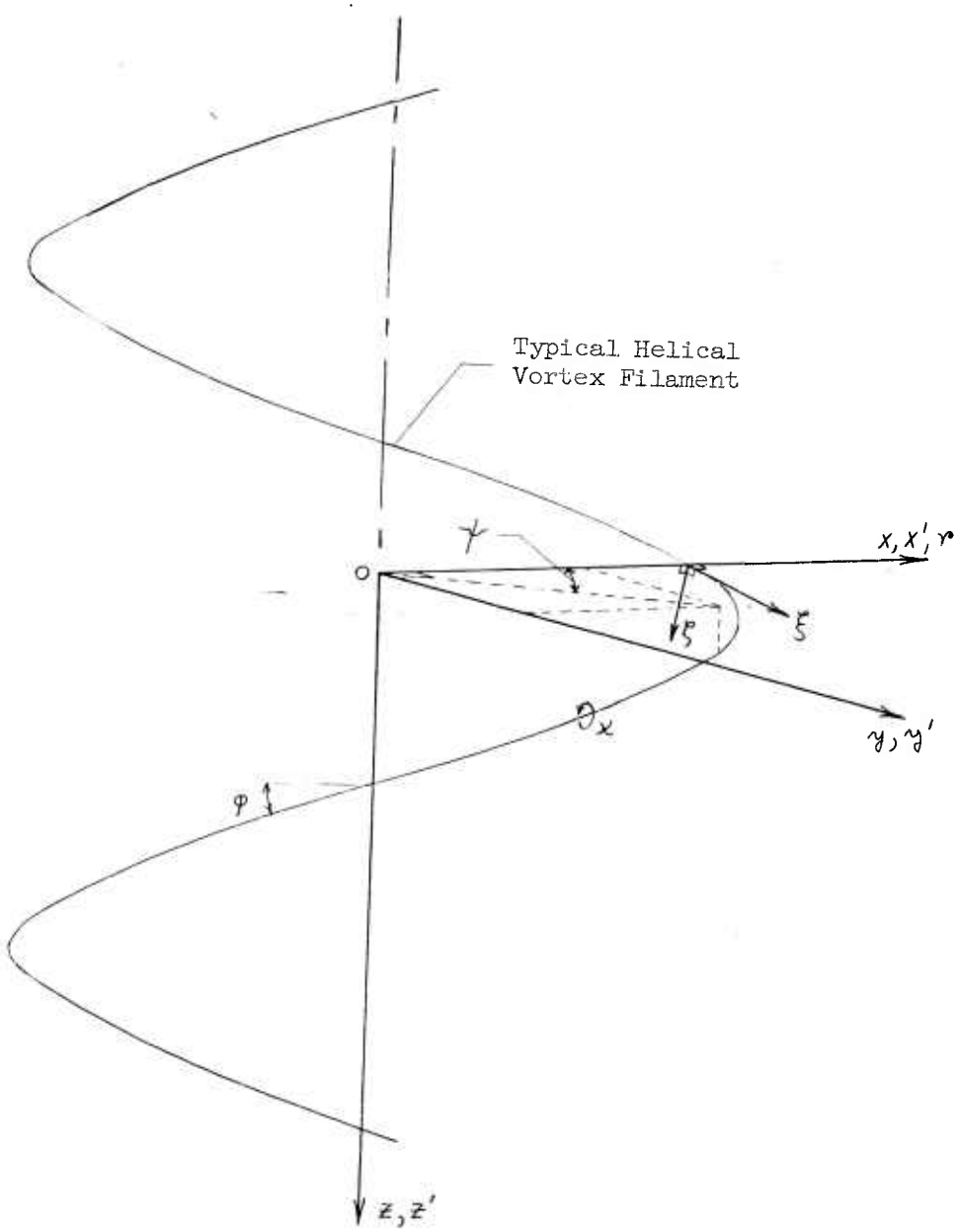


Figure 11. Coordinate Systems

where $\varphi'_m$ helix pitch angle in radians

Substituting into Equations 3 yield

$$u_x = -\sum_{m=1}^{M} \frac{\chi_m}{4\pi} \int \left\{ r' \tan\varphi' \left( r\sin\psi - r'\sin\psi' \right) - r'\cos\psi' \left( z - z_0' - r'\psi' \tan\varphi' \right) \right\}_m \frac{d\psi'}{P_m^3} \tag{6a}$$

$$u_y = \sum_{m=1}^{\infty} \frac{\chi_m}{4\pi} \int \left\{ r' \tan\varphi' \left( r\cos\psi - r'\cos\psi' \right) + r'\sin\psi' \left( z - z_0 - r'\psi' \tan\varphi' \right) \right\}_m \frac{d\psi'}{P_m^3} \tag{6b}$$

$$u_z = \sum_{m=1}^{M} \frac{\chi_m}{4\pi} \int \left\{ r'^2 - r r' \cos(\psi - \psi') \right\}_m \frac{d\psi'}{P_m^3} \tag{6c}$$

where $$P_m = \left\{ r^2 + r_m'^2 - 2 r r_m' \cos(\psi_m' - \psi) + \left( z - z_0' - r_m' - \psi_m' \tan\varphi_m' \right)^2 \right\}^{\frac{1}{2}} \tag{7}$$

The boundary conditions are more conveniently expressed in terms of the velocity components along the vortex sheet and perpendicular to the sheet. Thus,

$$u_r = u_x \cos\psi + u_y \sin\psi \tag{8a}$$

$$u_\xi = \left( u_y \cos\psi - u_x \sin\psi \right) \cos\varphi + u_z \sin\varphi \tag{8b}$$

$$u_\zeta = u_z \cos\varphi - \left( u_y \cos\psi - u_x \sin\psi \right) \sin\varphi \tag{8c}$$

where $u_r$ the radial velocity component

$u_\xi$ the component parallel to the vortex sheet and normal to the radial component

$u_\zeta$ the component normal to the vortex sheet and the radial component

$\varphi$ the helix pitch angle of the sheet at the point where the velocity components are to be calculated

The boundary conditions require that the radial velocity of each vortex filament making up the vortex system be zero; the normal component be proportional to the cosine of the helix pitch angle; and the tangential component be unspecified or immaterial. An additional requirement is that the line integral of the velocity taken about a path enclosing the wake be zero.

As far as is known, a solution of Equations 6 in terms of the elementary functions has not been found so that the solution becomes necessarily a numerical one. Thus, the vortex sheet is arbitrarily divided into a finite number of finite vortex filaments. The boundary conditions on the motion of the sheet must then be applied to points other than those corresponding to filament points for under such a circumstance Equation 7 may become zero and the integrands of Equations 6 become infinite. The calculating points for this analysis are chosen on the sheet and midway between the filaments for this reason. The equations to be numerically integrated are then as follows:

$$u_r = 0 = \sum_{m=1}^{M} \frac{\chi_m}{4\pi} \int_{-\infty}^{\infty} \left\{ r'^2 \tan\varphi' \sin(\psi'-\psi) + r'\left[z - z_0' - r'\psi' \tan\varphi'\right] \cos(\psi'-\psi) \right\}_m \frac{d\psi'}{P_m^3} \tag{9a}$$

$$u_\xi = \sum_{m=1}^{M} \frac{\chi_m}{4\pi} \int_{-\infty}^{\infty} \left\{ \left[ r' \tan\varphi' \left[ r - r' \cos(\psi'-\psi) \right] + r'\left(z - z_0' - r'\psi' \tan\varphi'\right) \sin(\psi'-\psi) \right] \cos\varphi + \left[ r'^2 - r r' \cos(\psi'-\psi) \right] \sin\varphi \right\}_m \frac{d\psi'}{P_m^3} \tag{9b}$$

$$u_\zeta = w\cos\varphi = \sum_{m=1}^{M} \frac{\chi_m}{4\pi} \int_{-\infty}^{\infty} \left\{ \left[ r'^2 - r r' \cos(\psi'-\psi) \right] \cos\varphi - \left[ r' \tan\varphi' \left[ r - r' \cos(\psi'-\psi) \right] + r'\left(z - z_0' - r'\psi' \tan\varphi'\right) \sin(\psi'-\psi) \right] \sin\varphi \right\}_m \frac{d\psi'}{P_m^3} \tag{9c}$$

where $W$ is the parameter describing the apparent axial motion of the wake vortex system.

The equations may be non-dimensionalized by dividing through by $W$. The two equations of interest are then:

$$\sum_{m=1}^{M} \frac{\chi_m}{4\pi R_0 W} \int_{-\infty}^{\infty} \left\{ x' \tan\varphi_0 \sin(\psi'-\psi) + x' \left[ \frac{z}{R_0} - \frac{z_0'}{R_0} - \psi' \tan\varphi_0 \right] \cos(\psi'-\psi) \right\}_m \frac{d\psi'}{P_m^3} = 0 \qquad (10a)$$

$$\sum_{m=1}^{M} \frac{\chi_m}{4\pi R_0 W} \int_{-\infty}^{\infty} \left\{ (x'^2 - \tan^2\varphi_0) + \left( \frac{x'}{x} \tan^2\varphi_0 - xx' \right) \cos(\psi'-\psi) \right.$$

$$\left. - \frac{x'}{x} \left[ \frac{z}{R_0} - \frac{z_0'}{R_0} - \psi' \tan\varphi_0 \right] \tan\varphi_0 \sin(\psi'-\psi) \right\}_m \frac{\cos\varphi \, d\psi'}{P_m^3} = \cos\varphi \qquad (10b)$$

where

$$x_m' = \frac{r_m}{R_0}$$

$$x = \frac{r}{R_0}$$

$$\tan\varphi_0 = x' \tan\varphi' = x \tan\varphi$$

$$P_m = R_0 \left\{ x^2 + x'^2 - 2xx' \cos(\psi'-\psi) + \left[ \frac{z}{R_0} - \frac{z_0'}{R_0} - \psi' \tan\varphi_0 \right]^2 \right\}^{\frac{1}{2}} \qquad (11)$$

$\varphi_0$ the pitch angle of the vortex filaments forming the wake boundary

$R_0$ wake radius

Computing Procedures

For the particular problem under consideration, it was convenient to divide the vortex system into two parts and to further sub-divide each part into an equal number of finite strength filaments. The helical vortex sheet was thus divided into ten equally spaced filaments, starting at the $x'_m = 0.05$ station and ending at the $x'_m = 0.95$ station for $z' = 0.0$. A portion of the boundary sheet was also divided into ten equally spaced filaments. Since the boundary sheet distribution will be periodic in the axial co-ordinate, the portion that was considered extended from the midpoint between adjacent helical sheets and on the wake boundary to the next midpoint in the negative axial direction. The inner helical vortex sheet spacing is given by

$$L = \frac{H}{b} = \frac{2\pi R_0 \tan \varphi_0}{b} \tag{12}$$

or non-dimensionally

$$\frac{L}{R_0} = \frac{2\pi \tan \varphi_0}{b} . \tag{13}$$

where L the axial spacing between successive inner helical vortex sheets

H the geometric pitch of the vortex filaments

b the number of blades in the propeller

Thus the wake boundary filaments were chosen to lie at $z'_m = \pm \frac{0.05H}{b}$, $\pm \frac{0.15H}{b}$, $\pm \frac{0.25H}{b}$, $\pm \frac{0.35H}{b}$, $\pm \frac{0.45H}{b}$ for $x' = 1.0$.

The calculating points were chosen midway between the filaments as follows: $x = 0.1, 0.2, 0.3, \cdots, 1.0$; $z = 0$ and $z = \pm \frac{0.1H}{b}, \pm \frac{0.2H}{b}$, $\pm \frac{0.3H}{b}, \pm \frac{0.4H}{b}, \pm \frac{0.5H}{b}$ ; $x = 1.0$. For the two-bladed wake, $\psi = 0, \pi$.

For the four-bladed propeller wake, $\psi = 0, \frac{\pi}{2}, \pi, \frac{3\pi}{2}$.

For given x, z, and $\psi$, the integrals of Equations 10 may be numerically evaluated for the given vortex filament geometry thereby yielding for this case of twenty filaments, forty equations with the filament strengths being the twenty unknowns. The resulting equations to be solved simultaneously are

$$\begin{bmatrix} A_{1,1} & A_{1,2} & A_{1,3} & \cdots & A_{1,20} \\ A_{2,1} & A_{2,2} & & & A_{2,20} \\ \vdots & & & & \vdots \\ A_{19,1} & & & & \vdots \\ A_{20,1} & A_{20,2} & \cdots & & A_{20,20} \\ B_{1,1} & B_{1,2} & \cdots & & B_{1,20} \\ B_{2,1} & & & & \vdots \\ \vdots & & & & \vdots \\ B_{20,1} & \cdots & & & B_{20,20} \end{bmatrix} \begin{bmatrix} \left(\frac{\varkappa}{4\pi R_0 w}\right)_1 \\ \left(\frac{\varkappa}{4\pi R_0 w}\right)_2 \\ \vdots \\ \left(\frac{\varkappa}{4\pi R_0 w}\right)_{20} \end{bmatrix} = \begin{bmatrix} 0 \\ 0 \\ \vdots \\ 0 \\ \omega_2 \varphi_1 \\ \omega_2 \varphi_2 \\ \vdots \\ \omega_2 \varphi_{20} \end{bmatrix} \tag{14}$$

where the "A"s are the evaluation of the integral in Equation 10a and the "B"s are the evaluations of the integral in Equation 10b. These forty equations were reduced to twenty normal equations by a least squares method. These twenty equations may be reduced to nineteen by applying the necessary condition that

$$\sum_{m=1}^{20} \left(\frac{\varkappa}{4\pi R_0 w}\right)_m = 0 \tag{15}$$

Thus the vortex filament strengths were found by solving the resulting nineteen simultaneous equations. (The twentieth value was found by substituting the nineteen values back into Equation 15.)

Computer Results

As a check on the analysis, the case for the two-bladed free propeller wake for $\tan \varphi_o = 0.5$ was computed and compared with the results of Reference 2. The comparison is presented in Table I and Figure 12 where it will be seen that the maximum difference in computed non-dimensional optimum blade bound vortex distribution is about 5 per cent. The source of this difference was not investigated because it was felt that for the present purposes, the agreement was satisfactory.

The first results for the non-dimensional optimum blade bound vortex distribution for a two-bladed shrouded propeller as determined by a numerical analysis is given in Table II. It will be noted that, although the computed distribution has the same general shape as that determined by measurement in the potential tank, the magnitudes are apparently in error by a factor of approximately 2 1/2. The probable reason for the discrepancy is discussed in the next section.

TABLE I

Comparison of Computed Non-dimensional Optimum
Blade Bound Vortex Distribution for a Two-Bladed Free Propeller

TAN $\varphi_o = 0.5$

| Station | Goldstein, Ref. 2 | Computer |
|---|---|---|
| 0.0 | 0.0 | 0.0 |
| .1 | .092 | .0905 |
| .2 | .175 | .1725 |
| .3 | .243 | .2405 |
| .4 | .295 | .2915 |
| .5 | .329 | .3235 |
| .6 | .341 | .3350 |
| .7 | .331 | .3250 |
| .8 | .295 | .2875 |
| .9 | .220 | .2090 |
| 1.0 | 0.0 | 0.0 |

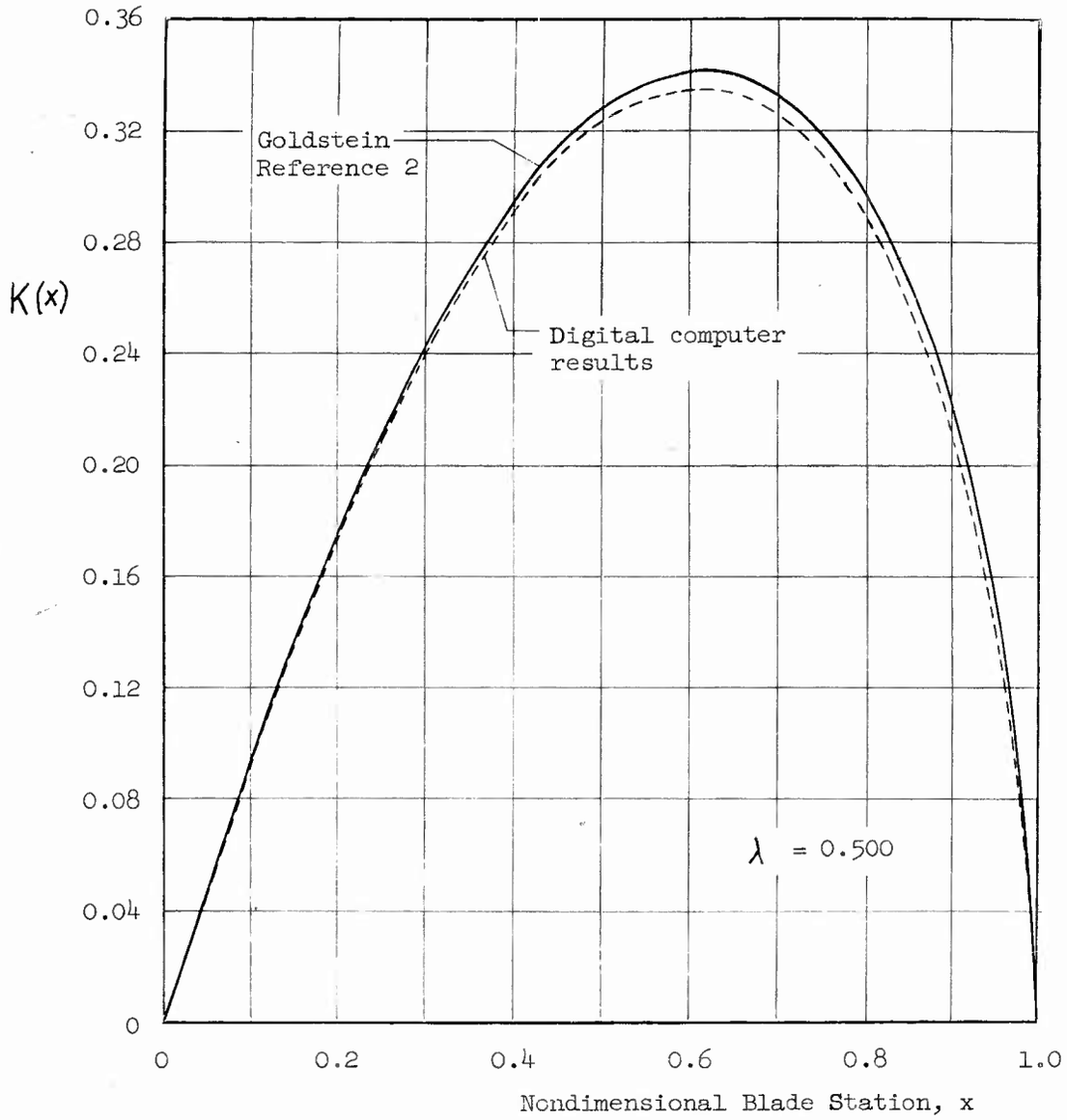


Figure 12. Comparison of two methods of computing the variation in nondimensional optimum blade bound vortex distribution with blade station for free propellers.

TABLE II

Computed Non-dimensional Blade Bound Vortex

Distribution for a Two-Bladed Single-Rotation Shrouded Propeller

Tan $\varphi_o = 1.356$

| x | Computed | Measured |
|---|---|---|
| .05 | .0269 | .012 |
| .15 | .0776 | .036 |
| .25 | .1337 | .061 |
| .35 | .1862 | .087 |
| .45 | .2375 | .111 |
| .55 | .2872 | .132 |
| .65 | .3350 | .148 |
| .75 | .3798 | .164 |
| .85 | .4196 | .174 |
| .95 | .4503 | .180 |

## DISCUSSION

### Methods of Obtaining Design Parameters

Both the potential tank approach and the digital computer approach have advantages and disadvantages. The primary advantage of the potential tank method is that after the model construction has been completed and the electrical apparatus has been assembled, the measurement of the desired quantities may be accomplished with relative ease. The accuracy of the results is directly associated with the accuracy of the model construction, but the effects of small geometric inaccuracies on the measured quantities may be made small by making the surveys at a number of stations and taking the arithmetic average of the station data. The greatest disadvantage of this method lies in the model construction. Using the techniques previously discussed, a usable helical surface having a geometric pitch less than the 1.356 used in the experiments could not be obtained although considerable time was spent trying to do so. The cementing of the helix into the tube was also a time-consuming process. It is believed that additional development of the forming techniques will be required if this approach is to be used to obtain the necessary design parameters.

The digital computer approach is almost at the opposite extreme. The mathematical model of the wake vortex system may be easily formulated and its geometry may be made as "exact" as is required. However, it is necessary to replace the continuous distribution of vorticity in the wake with an approximate system composed of a finite number of finite strength vortex filaments. The integration itself, being numerical, introduces some error. It appears from the results presented, that these approximations may have introduced errors which were magnified out of all proportion in the particular method used to obtain the simultaneous solution of the equations for the strengths of these vortex filaments. The distribution of bound vortex strength so obtained seems to be dependent upon which filament is eliminated in satisfying the requirement of Equation 15. The

usual tests were applied to the determinants obtained from the array of simultaneous equations and it was shown that this determinant was "well-behaved".

It has been previously mentioned that the shape of the computed distribution agreed qualitatively with the measured distribution, but that the magnitude was greater by a factor of about 2 1/2. Considerable time was spent in trying to determine the origin of this apparent factor but no conclusion could be reached within the allowable time and financial limitations. This difference was totally unexpected since the program as written for the computer had yielded results which compared closely with published results for lightly-loaded free propellers, as is shown in Table I and Figure 12.

The question arose as to which of the two distributions was most likely to be correct. On comparison with the theoretical distribution for an infinite number of blades, as shown in Figure 10, it was reasoned that the calculated results were in error because these latter computed values exceeded the theoretical values for the infinite number of blades by an appreciable factor. The computed mass coefficient or total velocity loss factor $\mu$ also exceeded that of the infinite number of blades. The measured distribution and computed mass coefficients for the two- and four-bladed propellers, however, indicated the same qualitative comparison with the infinite number of blades as for the free propeller cases of Reference 3; that is, the finite number of blades cases yielded lower mass coefficients than that of the infinite bladed propeller. For this reason, it is believed that the measured distributions are representative of the bound vortex distribution of shrouded, lightly-loaded, single-rotation propellers having a finite number of blades.

In spite of the inconclusiveness of the computer results, it is believed that this approach would be the most efficient means of determining the necessary design parameters. The first step in a continuation of this approach would be to obtain an independent check on the coefficients appearing in the array of simultaneous equations. This has not been done because of the time and financial limitations. A second or concurrent step would be to increase the number of filaments considered and to compare

the resulting vortex distribution with that of the original computation. A third possibility would involve a slightly different mathematical model in which the desired distribution is expressed as a Fourier Series and instead of solving simultaneously for the ordinates of the distribution curve, the Fourier coefficients would be determined. This latter approach has proved to be advantageous in the calculation of three-dimensional spanwise wing loadings and may offer the same advantages in this case.

Methods of Presenting Design Parameters

In order to cover the range of advance ratios and number of blades which are likely to be of interest, it is suggested that any continuation of this investigation should determine the optimum bound vortex distribution for shrouded propellers having from two to five blades both single- and dual-rotation and for a range of wake helix pitch angle $\varphi_o$ from about 10° to about 70°. These results could be presented in the form of tables and charts in which $K(x)$ is plotted versus blade non-dimensional radius $x$ for various wake advance ratios $\lambda = \tan \varphi_o$. In addition, it would be necessary to determine from these distributions, the mass coefficient $\varkappa$; the axial loss coefficient $\epsilon$; and their ratio, $\frac{\epsilon}{\varkappa}$. These parameters could also be presented in the form of tables and charts as plotted versus advance ratio $\lambda$ for various numbers of blades. With these charts available and for correctly designed shrouds, the design of the optimum propeller becomes a straightforward process as indicated in Appendix IV.

## CONCLUSIONS AND RECOMMENDATIONS

The potential tank approach will yield by direct measurement the parameters necessary for designing optimum shrouded propellers, but it has an inherent disadvantage in that the construction of sufficiently accurate models is difficult and time consuming and further development of the construction and forming techniques would probably be required for models having a lower pitch than about 50°.

The results obtained from the first digital computer attempt to determine the bound vortex distribution were unsatisfactory. Due to limitations on time and funds, it was not possible to resolve the discrepancies. However, it is believed that the digital computer approach would in the long run be more efficient. Thus, it is recommended that the digital computer approach be used in any extension of the present work.

## APPENDIX I

## VORTEX SYSTEM

The argument as to the geometry and motion of the wake vortex pattern of an optimum shrouded single-rotation propeller is essentially the same as that presented by Betz in reference 1 and Theodorsen in reference 3. Following these approaches, consider a non-optimum shrouded propeller which is producing the required thrust at the expenditure of the necessary amount of power. At a distance behind this first shrouded propeller system such that the shroud interference velocities are negligible, arrange a second shroud-propeller having the same number of blades and rotational speed as the first propeller and so phased with the first propeller that each blade intercepts one of the sheets of discontinuity that is shed from the former propeller's blade trailing edges. The diameter of the shroud of this second system is set equal to the wake diameter so that it intercepts the sheet of discontinuity that is shed from the first shroud's trailing edge. Assume that the second propeller is mounted on an extension of the shaft of the first propeller and assume further that neither the second propeller nor the shroud contribute to the motion of the wake nor disturb the flow in any way. Similarly place a third shrouded propeller, et cetera, until a large number of shrouded propellers are arranged in tandem, all mounted on the shaft of the first propeller, all having the required phase relation, and none contributing to the motion of the wake nor to the thrust or power required.

In general, certain of the blade elements of the first propeller will be operating at relatively high efficiencies while other elements will be operating at relatively low efficiencies. This will be evident in the wake, as will be seen later, by the pitch of the wake spiral; the efficiency being higher where the pitch is lower and vice versa. Suppose now that on the second shrouded propeller, a positive increment of thrust is added to a blade element operating in a region where the pitch of the helical vortex sheet is low and an equal increment of negative thrust is added on the third propeller to an element operating

in a region where the pitch is high. The thrust of the complete system remains unchanged but the third propeller adds more power to the shaft by acting as a windmill than the second propeller requires to produce the thrust increment so that a net reduction of the power required by the system is realized. (Of course skin friction is neglected and it is assumed that the thrust increments are very small so that the power recovery factor is 100%.) The efficiency of these added increments may be obtained by considering figure I-1:

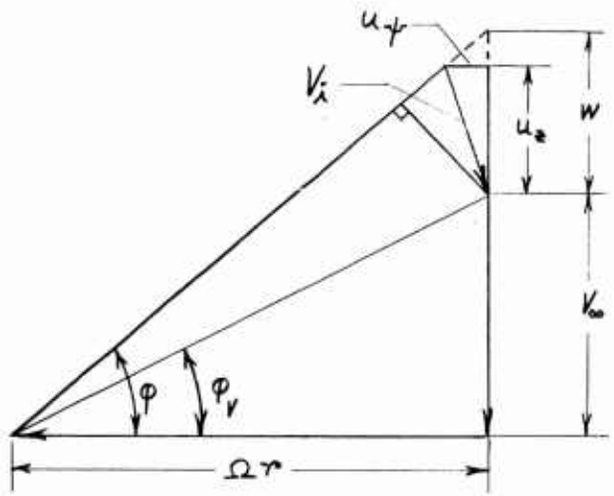


Figure I-1. Velocity diagram in the ultimate wake.

Using the Kutta-Joukowski theorem, the increment in thrust is

$$\Delta T = \rho \Delta \Gamma (\Omega r - u_\psi)$$

where $\Delta T$ the increment in thrust

$\rho$ fluid density

$\Delta \Gamma$ the increment in bound vortex strength

$\Omega$ the propeller rotational velocity

$r$ the radius at which the increment in thrust is added

$u_\psi$ the component of the induced velocity $V_i$ in the plane of rotation

The increment in torque is

$$\Delta Q = \rho \Delta \Gamma \left( V_\infty + u_z \right) r$$

where

$\Delta Q$ the increment in torque

$V_\infty$ the velocity along the flight path

$u_z$ the axial component of the induced velocity

This gives for the efficiency, $\eta$

$$\eta = \frac{V_\infty \Delta T}{\Omega \Delta Q} = \frac{\rho \Delta \Gamma (\Omega r - u_\psi) V_\infty}{\rho \Delta \Gamma (V_\infty + u_z) \Omega r}$$

$$= \left( \frac{V_\infty}{V_\infty + w} \right) \left( \frac{\Omega r - u_\psi}{V_\infty + u_z} \right) \tan \varphi$$

$$= \frac{V_\infty}{V_\infty + w}$$

$$= \frac{1}{1 + \overline{w}} \qquad (I-1)$$

where

$$\overline{w} = \frac{w}{V_\infty}$$

and $w$ the parameter describing the apparent axial motion of the wake vortex spiral

The elemental efficiency is thus simply a function of the ratio of the apparent axial velocity of the helical vortex sheet element to the free stream velocity. The aforementioned process of adding an increment of

thrust on a blade element of one propeller and removing the same amount on the following propeller with a net reduction in power required is continued until no further reduction is realized. At this point the efficiency of the added element of thrust will be the same regardless of the radius at which it is added. From equation I-1 this occurs when the parameter $\overline{w}$ is the same at each blade station for the last propeller in the array. The wake behind this last propeller represents the wake for the optimum case. The problem now becomes the determination of the single propeller-shroud combination which will yield the same wake configuration as the array.

The preceeding analysis shows that the optimum condition is obtained when the ultimate wake vortex pattern appears to move as a rigid body and the pitch of the inner helical wake spiral is constant along the radius. Unfortunately no other information is obtained about the geometry unless some additional assumptions are made about the disturbance velocities associated with the shroud. For this analysis, it will be assumed that the system is lightly loaded so that shroud disturbance velocities are such that the wake has reached its ultimate configuration at the shroud trailing edge and that the geometric pitch of the helical wake spiral is constant. In addition, each vortex filament of the inner helical sheet will intercept the same radial coordinate lines. Therefore the wake geometry and motion are completely specified and will appear as described below.

Consider a two-bladed, single-rotation shrouded propeller and the induced flow field that is associated with the vortex sheet that is shed from the blade trailing edges. Without the shroud, the induced flow field would be approximately as sketched in figure I-2 for the vicinity of the shroud trailing edge.

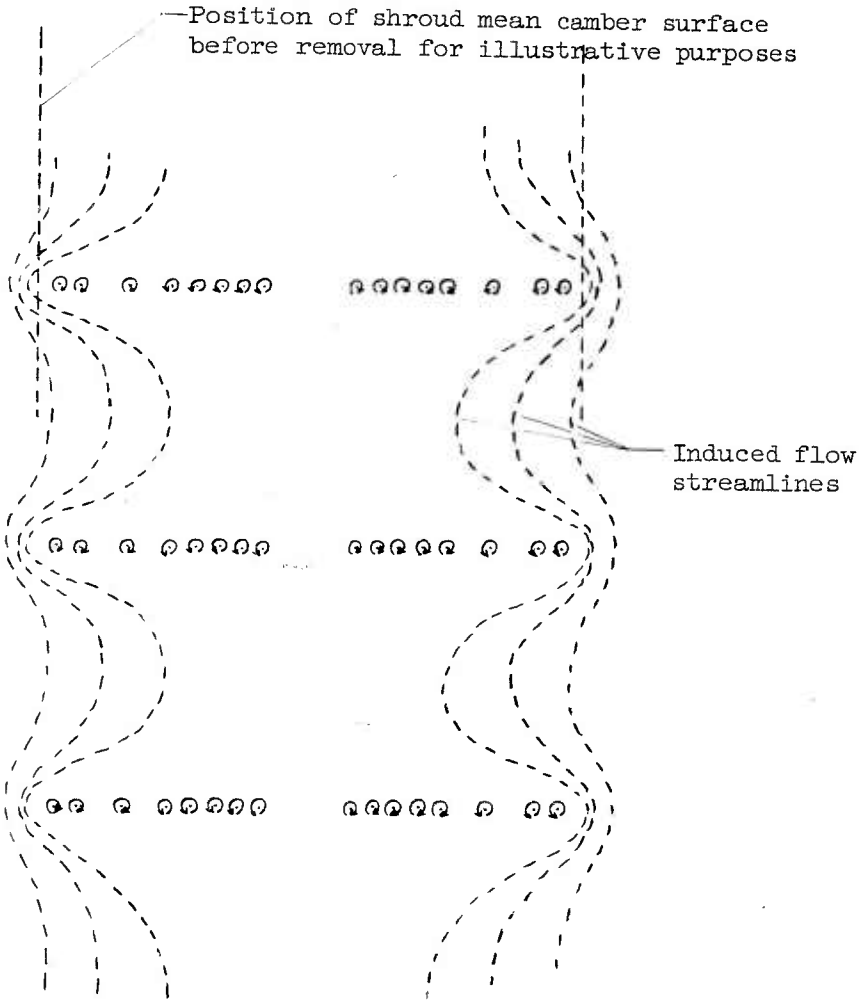


Figure I-2. Cross-section of wake vortex system of a two-bladed single-rotation propeller in the vicinity of the shroud trailing edge. Shroud is removed from the flow for illustrative purposes.

It may be seen from the figure that such a trailing blade vortex system has associated with it, regions having large radial induced velocity components and that with respect to a reference system fixed in the shroud position, this flow is periodic. In order for the shroud mean camber surface to correspond to a streamline, it is necessary that a distribution of vorticity be placed along the shroud mean camber surface in such a manner as to cancel out all velocity components normal to this surface. Since the radial velocities that are associated with the vortex sheet change with time when measured with respect to the shroud, then that part of the shroud bound vortex distribution which cancels out these radial components must also be periodic in nature and a function of the number of blades in the propeller. This part of the shroud bound vortex system may be considered to rotate with the propeller but for present purposes does not contribute to the wake boundary vortex system. The non-rotating components of the shroud bound vortex system are considered to be circular rings bound to the shroud mean camber surface as shown in figure I-3.

The wake boundary vortex system is comprised of the continuations of the vortex filaments that are shed from the blade trailing edge which in turn represent the changes in the blade bound vortex strength with radial position along the blade. Thus the blade bound vortex at the blade tip is considered to be continued into the shroud contour where it is spread out on the shroud mean camber surface as depicted in figure I-3. While within the contour, it is assumed that all of the necessary adjustments in phase relationship with the blade trailing vortex system occur so that the motion of the wake boundary vortex system is along the tangent to the shroud mean camber surface at the trailing edge.

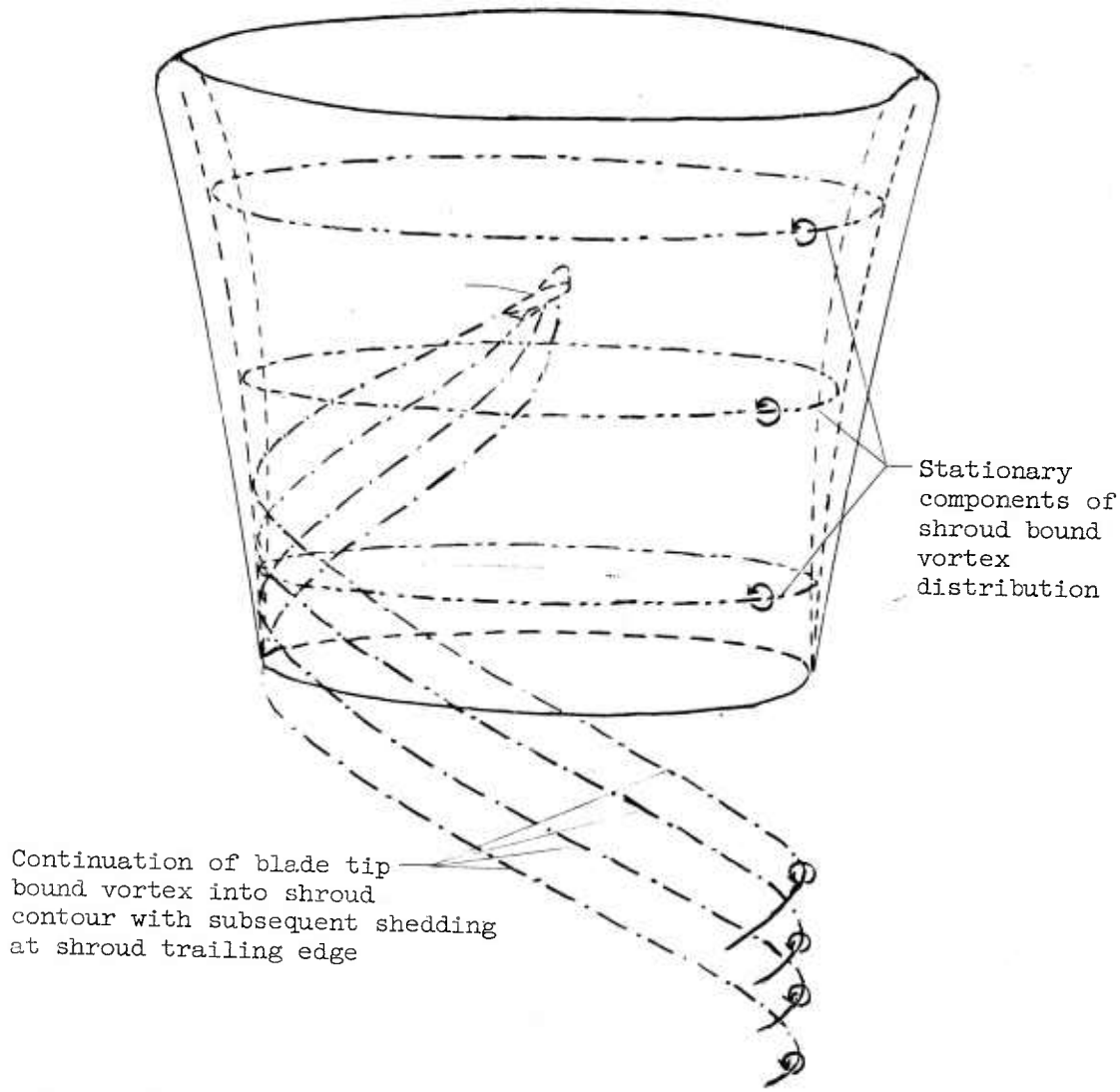


Figure I-3. Vortex system on shroud mean camber surface showing non-rotating components of shroud bound vortex distribution and the continuation of the blade tip bound vortex into the shroud contour with its subsequent spreading out and shedding at the shroud trailing edge as the wake boundary vortex system.

To simplify the illustration, it will be assumed that the shroud is so designed (i.e. long enough) that the wake has achieved its ultimate configuration at the plane of the shroud trailing edge. Thus in order that no further distortion of the wake take place, there must be shed from the shroud trailing edge a cylindrical sheet of vorticity of the proper distribution and phase relationship with respect to the blade sheet so as to fulfill this condition, (i.e. velocity vector must be tangent to shroud mean camber surface at the trailing edge.) The motion of these vortex systems for the lightly-loaded case must be the same as that of a nut on a screw where the shroud trailing sheet corresponds to the thread on the nut and the blade trailing sheet corresponds to the thread on the screw. It is to be noted that such a system will always maintain the proper phase relationships while having different rotational velocities (all the necessary adjustments in configuration having taken place within the shroud). There is, of course, then no further change in the distribution of vorticity with respect to the helical coordinates defined by the vortex filament. It is believed that a cross-section of the optimum shrouded-propeller wake vortex system will be somewhat as indicated schematically in figure I-4 for the two-bladed case. It is this configuration that is considered in the analyses of this report.

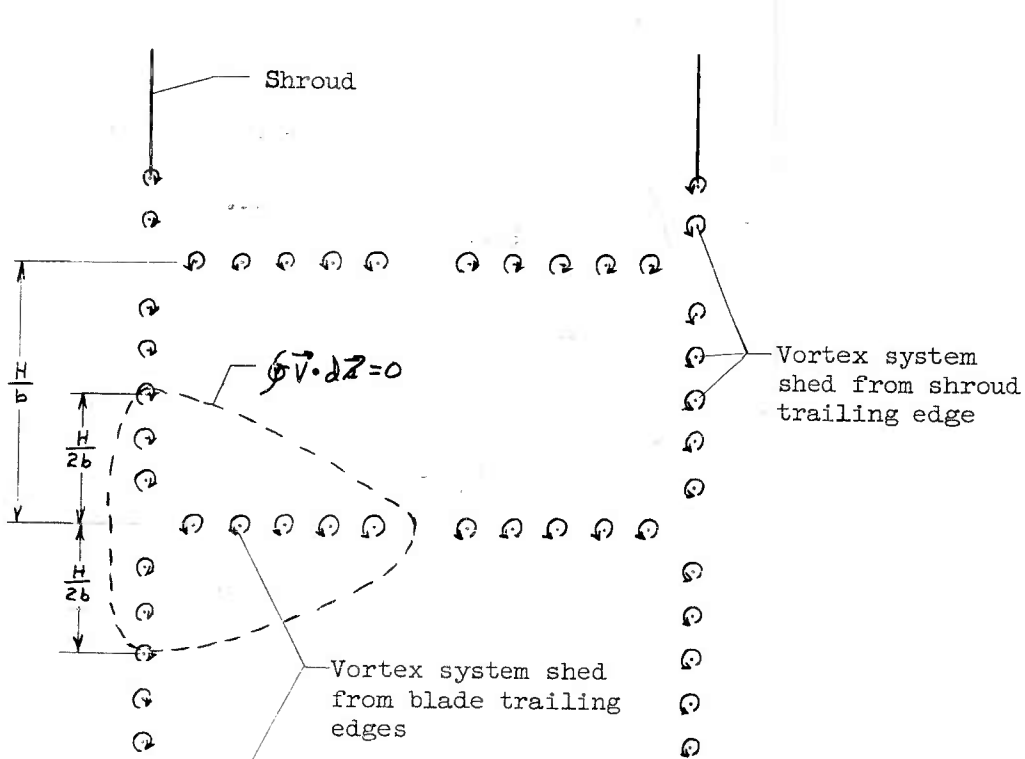


Figure I-4. Cross-section of the vortex system of a two-bladed, single-rotation, shrouded propeller as visualized for the analyses of this report.

## APPENDIX II

## CALCULATION OF THRUST AND POWER

Using the momentum theorem and considering the control volume shown in figure II-1,

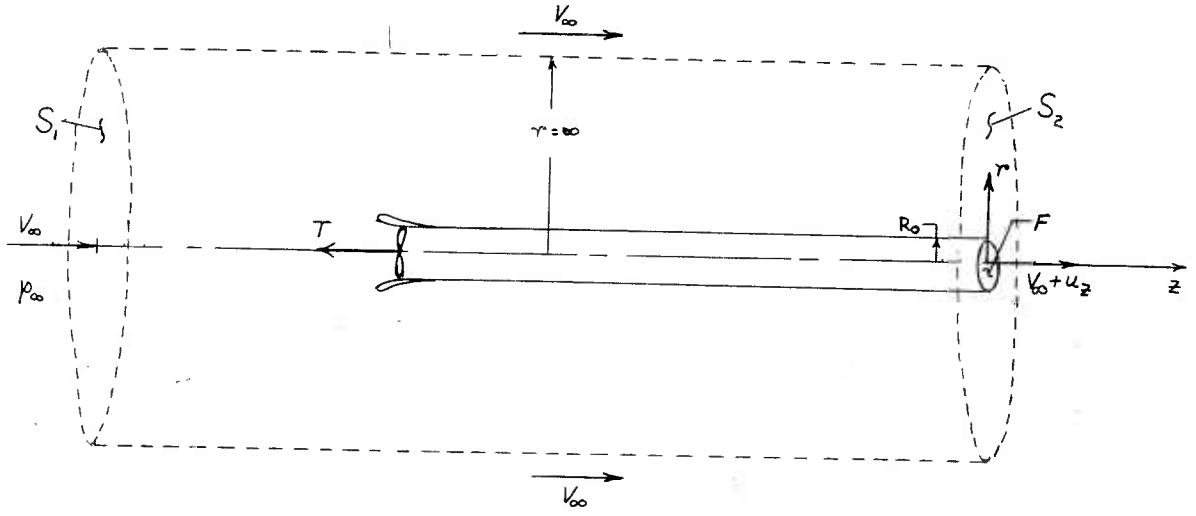


Figure II-1. Control volume used in determining the thrust.

the thrust is found by considering the average pressure forces acting on the control surface and the average time rate of change of momentum of the fluid within the control surface. This average is taken over a time $\Delta t = 2\pi/b\Omega$ and the integration is with respect to time $dt = dz/(V_\infty + w)$ so that

$$T + \frac{1}{\Delta t}\int_{S_1,S_2} p\, dt\, dS = \frac{1}{\Delta t}\int_2 \rho(V_\infty + u_z)\, dt\,(V_\infty + u_z)\, dS_2 - \frac{1}{\Delta t}\int_1 \rho V_\infty\, dt\, V_\infty\, dS_1$$

or

$$T + \frac{b\Omega}{2\pi(V_\infty + w)}\int_{VOL}(p_\infty - p)\, dz\, dS = \frac{b\Omega\,\rho}{2\pi(V_\infty + w)}\int_{VOL}\left(V_\infty u_z + u_z^2\right) dz\, dS \qquad (II-1)$$

since $V_\infty \, dS_1 = (V_\infty + u_z) \, dS_2$

where

| | |
|---|---|
| $T$ | thrust on propeller-duct system, lbs |
| $b$ | number of blades |
| $V_\infty$ | undisturbed, free-stream velocity, ft/sec |
| $w$ | apparent axial movement of wake helix with respect to a point fixed in space, ft/sec |
| $\Omega$ | rotational velocity of propeller, radians/sec |
| $p_\infty$ | undisturbed, free-stream static pressure, lbs/sq. in. |
| $p$ | static pressure, lbs/sq. in |
| $z$ | coordinate along wake axis, positive in opposite direction to propeller thrust, ft. |
| $S$ | control surface area, $ft^2$ |
| $\rho$ | fluid density, $slugs/ft^3$ (incompressible) |
| $u_z$ | axial component of the induced velocity, ft/sec |
| $t$ | time, sec. |

Before equation II-1 may be integrated, an expression must be found which relates the local static pressure to the local velocity. This required expression may be obtained as follows by integrating Euler's equations of motion along a path in a frictionless, homogeneous, irrotational, incompressible, unsteady flow field. Since a velocity potential $\phi$ exists, the $x$-component of Euler's equation may be written

$$\frac{\partial}{\partial \tau}\left(\frac{\partial \phi}{\partial x}\right) + u \frac{\partial u}{\partial x} + v \frac{\partial u}{\partial y} + w \frac{\partial u}{\partial z} = -\frac{1}{\rho} \frac{\partial p}{\partial x}$$

Multiplying by $dx$ and imposing the irrotationality condition that $\frac{\partial u}{\partial z} = \frac{\partial w}{\partial x}$, $\frac{\partial u}{\partial y} = \frac{\partial v}{\partial x}$, the following is obtained

$$\frac{\partial^2 \phi}{\partial x \partial \tau} dx + u \frac{\partial u}{\partial x} dx + v \frac{\partial v}{\partial x} dx + w \frac{\partial w}{\partial x} dx = -\frac{1}{\rho} \frac{\partial p}{\partial x} dx$$

Multiplying the $y$- and $z$-components of Euler's equations by $dy$ and $dz$ respectively, imposing the condition of irrotationality, adding the three

resulting scalar equations and integrating gives the desired expression.

$$\frac{\partial \phi}{\partial t} + \frac{p}{\rho} + \frac{1}{2} V^2 + f(t) = \text{CONSTANT} \qquad (II-2)$$

Considering first the region outside the wake, there can be no induced velocity at $r = \infty$ so that $\left(\frac{\partial \phi}{\partial t}\right)_{r=\infty} = 0$ ; $[f(t)]_{r=\infty} = 0$ so that

$$\frac{\partial \phi}{\partial t} + \frac{p}{\rho} + \frac{1}{2} V^2 + f(t) = \frac{p_\infty}{\rho} + \frac{1}{2} V_\infty^2 = \frac{p_{o_1}}{\rho} \qquad (II-3)$$

where $p_{o_1}$ is the stagnation pressure in the undisturbed flow. The region within the wake boundaries is not so simple and additional relations must first be found.

Consider a helical coordinate system $r, \xi, \zeta$ which is defined in terms of the cylindrical coordinates $r, \psi, z$ as follows so that for the instant under consideration, the helical vortex sheet coincides with the $\zeta = 0$ surface.

$$\left.\begin{aligned} r &= r & 0 \le r \le \infty \\ \xi &= r\psi \cos\varphi + z \sin\varphi & -\infty \le \xi \le \infty \\ \zeta &= -r\psi \sin\varphi + z\cos\varphi & -\frac{(V_\infty + w)\cos\varphi}{2b\left(\frac{\Omega}{2\pi}\right)} \le \zeta \le \frac{(V_\infty + w)\cos\varphi}{2b\left(\frac{\Omega}{2\pi}\right)} \end{aligned}\right\} (II-4)$$

where $\xi$ is measured along the helical vortex filaments; $\zeta$ is measured along a helical line that is normal to the vortex filaments and $\varphi$ is the helix pitch angle of the $\zeta = \text{CONST.}$ coordinate lines.

Due to helical symmetry, the disturbance velocity vector is constant along helical lines $r = \text{CONST.}$, and $\zeta = \text{CONST.}$ both inside and outside of the wake. Therefore

$$u_r = \frac{\partial \phi}{\partial r} = f_r(r, \zeta)$$

$$u_\xi = \frac{\partial \phi'}{\partial \xi} = f_\xi(r, \xi)$$

$$u_\zeta = \frac{\partial \phi'}{\partial \zeta} = f_\zeta(r, \zeta)$$

where $\phi'$ is the induced velocity potential.

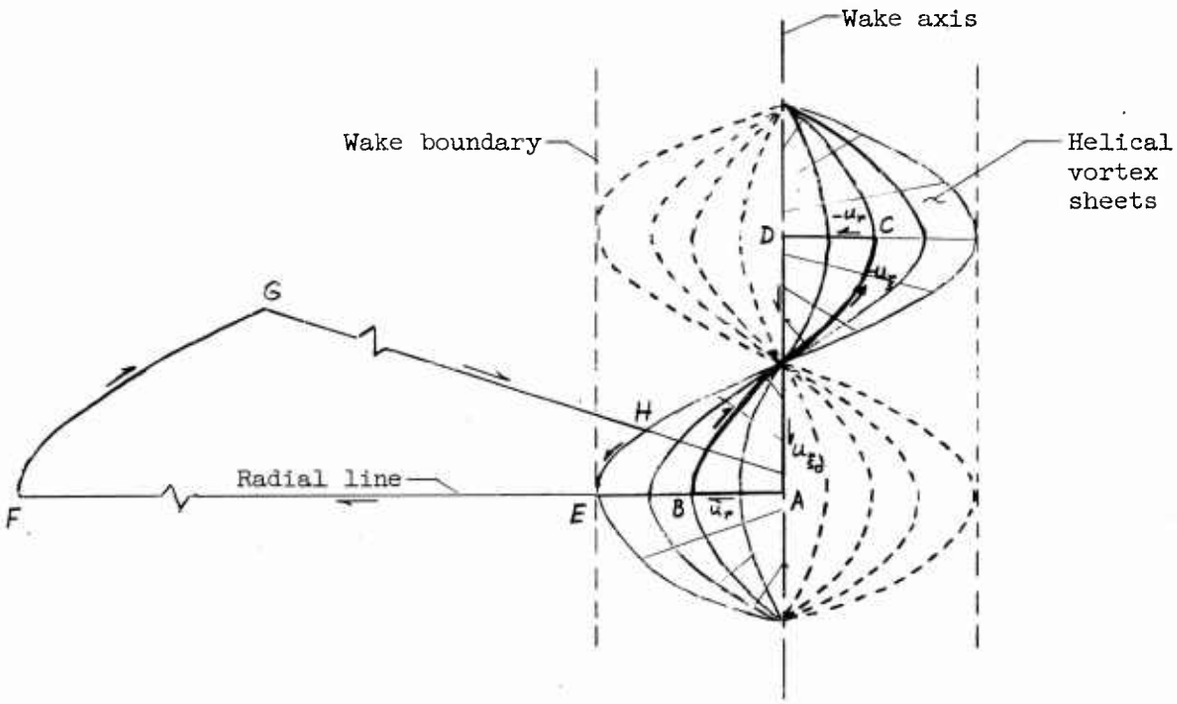


Figure II-2. Wake vortex system showing the various paths along which the line integrals are calculated.

Consider the line integral of the velocity along the path $\overline{ABCDA}$ within the wake as shown in figure II-2. The line $\overline{BC}$ is a helical line along which both $r$ and $\zeta$ are constant so that $u_\xi$ is constant. The lines $\overline{AB}$ and $\overline{CD}$ are radial lines such that the same helical lines, $r$ = CONSTANT and $\zeta$ = constant, intersect both lines. The line $\overline{DA}$ coincides with the axis of the wake. Since no vorticity is enclosed by

the lines, the line integral should be zero.

$$\int_A^B u_r\,dr + \int_B^C u_\xi\,d\xi + \int_C^D u_r\,dr + \int_D^A u_\xi\,d\xi = 0$$

But $u_r(r,\xi)_{AB} = u_r(r,\xi)_{DC}$ so that $\int_A^B u_r\,dr + \int_C^D u_r\,dr = 0$ and the remaining terms give

$$u_\xi(\xi_C - \xi_B) + u_{\xi_o}(z_A - z_D) = 0$$

assuming that $u_{\xi_o}$ is different from zero.

From equation II-4

$$\xi_C - \xi_B = (r\psi_C\cos\varphi + z_C\sin\varphi) - (r\psi_B\cos\varphi + z_B\sin\varphi)$$

and if

$$\psi_B = 0\ ;\ z_A = z_B = 0\ ;\ \text{THEN}\ \psi_C = -\frac{2\pi}{b}\ ;\ z_D = z_C = -\frac{V_\infty + w}{b\left(\frac{\Omega}{2\pi}\right)}$$

then

$$-u_\xi\left[r\frac{2\pi}{b}\cos\varphi + \frac{V_\infty + w}{b\left(\frac{\Omega}{2\pi}\right)}\sin\varphi\right] + u_{\xi_o}\frac{V_\infty + w}{b\left(\frac{\Omega}{2\pi}\right)} = 0$$

$$u_\xi = \frac{u_{\xi_o}\frac{V_\infty + w}{\Omega}}{r\cos\varphi + \frac{V_\infty + w}{\Omega}\sin\varphi} = \frac{u_{\xi_o}}{\frac{\Omega r}{V_\infty + w}\cos\varphi + \sin\varphi}$$

$$u_\xi = u_{\xi_o}\sin\varphi \qquad (\text{II} - 5a)$$

Consider next the line integral of the velocity along the path $\overline{EFGHE}$ outside the wake as shown in figure II-2. The line $\overline{HE}$ is a helical line on the outer surface of the cylindrical sheet of vorticity and is parallel to the vortex filaments. The lines $\overline{EF}$ and $\overline{GH}$ are radial lines such that the same helical coordinate lines, $r = \text{CONST.}$ , $\xi = \text{CONST.}$ intersect both lines so that $u_r(r,\xi)_{EF} = u_r(r,\xi)_{GH}$ . The line $\overline{FG}$ is a helical line at $r = \infty$ . As no vorticity is enclosed by the line, the line integral is again zero.

$$\int_E^F u_r\,dr + \int_F^G u_\xi\,d\xi + \int_G^H u_r\,dr + \int_H^F u_{\xi_R}\,d\xi = 0$$

Since $u_{\xi_{R_o}}$ is parallel to the vortex filaments on the surface of the cylinder, there can be no discontinuity in this velocity component so that $u_{\xi_{R_o^-}} = u_{\xi_{R_o^+}} = u_{\xi_o} \sin \varphi_{R_o}$ , where $\varphi_{R_o}$ is the helix pitch angle of the boundary wake filaments. Again

$$\int_E^F u_r \, dr + \int_G^H u_r \, dr = 0$$

and

$$u_\xi (\xi_G - \xi_F) + u_{\xi_o} \sin \varphi_{R_o} (\xi_E - \xi_H) = 0$$

If

$$\psi_{FE} = 0 \; ; \; z_F = z_E = 0 \; ; \; \text{THEN} \; \psi_{GH} = -\psi \; ; \; z_G = z_H = -\frac{V_\infty + w}{\left(\frac{\Omega}{\psi}\right)}$$

and

$$-u_\xi \left[ r\psi \cos\varphi + \frac{V_\infty + w}{\left(\frac{\Omega}{\psi}\right)} \sin\varphi \right] + u_{\xi_o} \sin\varphi_{R_o} \left[ R_o \psi \cos\varphi_{R_o} + \frac{V_\infty + w}{\left(\frac{\Omega}{\psi}\right)} \sin\varphi_{R_o} \right] = 0$$

$$u_\xi = \frac{u_{\xi_o} \sin\varphi_{R_o} \left[ R_o \cos\varphi_{R_o} + \frac{V_\infty + w}{\Omega} \sin\varphi_{R_o} \right]}{r\cos\varphi + \frac{V_\infty + w}{\Omega} \sin\varphi}$$

$$u_\xi = u_{\xi_o} \sin\varphi \qquad \text{(II-5b)}$$

But $\tan\varphi = \left(\frac{R_o}{r}\right) \tan\varphi_{R_o}$ so that as $r \to \infty$ ; $\varphi \to 0$ and the conditions on $u_\xi$ at infinity are satisfied.

It has been shown in Appendix I that the optimum condition requires that the vortex system move to the rear as a solid body. Equations II-5 show that this condition is fulfilled and the total induced velocity at the helical sheet and cylindrical helical sheet vortex filaments is constant and equal to $u_{\xi_o}$ . Thus at each vortex filament

$$u_\xi = u_{\xi_o} \cos\varphi \qquad \text{(II-6)}$$

and the entire field pattern moves axially with a velocity, $u_{\xi_o}$ . For other points in the flow however

$$u_r = f_r(r, \xi)$$

$$u_\xi = u_{\xi_o} \sin\varphi$$

$$u_\xi = f_\xi(r, \xi)$$

There is another condition which these results must satisfy and that is that the line integral about a path enclosing the wake must be zero for, if this is not true, the velocity potential would be multi-valued outside the wake. Consider a helical path $r = R_0$ ; $\xi = \text{CONST.}$ which lies on the outside of the wake boundary as shown in figure II-3. The helical path

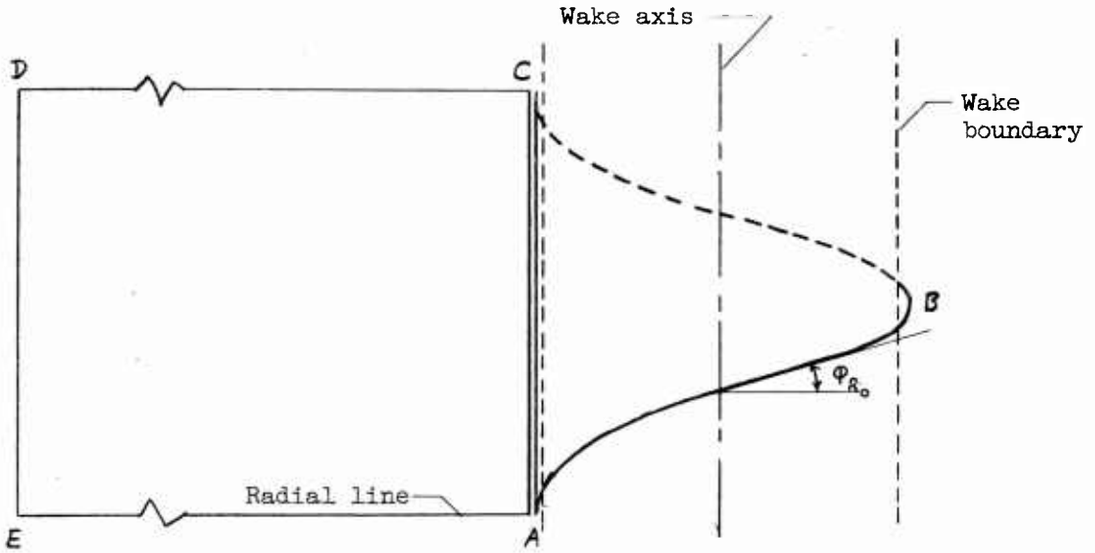


Figure II-3. Paths along which line integrals must be evaluated to show that the line integral about a path enclosing the wake is zero.

$\overline{ABC}$ is closed by a line $\overline{CA}$ parallel to the wake axis. The velocity component $u_\xi$ along $\overline{ABC}$ is constant and equal to $u_{\xi_0} \sin \varphi_{R_0}$. The length of the path $\overline{ABC}$ is $2\pi R_0 \sec \varphi_{R_0}$ so that

$$\int_C^A u_z \, dz + 2\pi R_0 u_{\xi_0} \tan \varphi_{R_0} = 0$$

Next consider the path $\overline{ACDE}$. Due to helical symmetry, the line integral along $\overline{CD}$ is equal and opposite to the line integral along $\overline{EA}$, and

$$\int_A^C u_z\,dz + \int_D^E u_z\,dz = 0$$

But if the line $\overline{DE}$ is allowed to approach $r=\infty$, $u_{z_\infty} = 0$ AND $\int_A^C u_z\,dz = 0$. Therefore

$$\oint_{ABCA} \vec{V}\cdot d\vec{s} = 2\pi R_0 u_{\xi_0} \tan\varphi_{R_0}$$

and the flow pattern (i.e. a system of vortex filaments having the same geometric pitch) is not possible unless $u_{\xi_0} = 0$. If the axial velocity is zero along the wake axis, then $u_\xi$ is zero everywhere. Thus the induced velocity is everywhere normal to the $r$ = CONSTANT, $\xi$ = CONSTANT lines and at the vortex filaments,

$$u_\xi = w\cos\varphi$$

where $w$ is a parameter which, along with the free stream velocity $V_\infty$, determines the geometric pitch of the helical vortex system. The vortex system will again appear to move as a solid body but actually there will be relative motion between the fluid particles in adjacent vortex filaments.

The induced velocity component $u_\xi$ will be continuous everywhere except across the cylindrical boundary of helical vortex filaments where the change in the value of this component is equal to the sheet strength $\Gamma(\xi)$. Thus

$$\Gamma(\xi) = u_{\xi_{R_0^-}} - u_{\xi_{R_0^+}} \qquad (II-7)$$

where $u_{\xi_{R_0^-}}$ is the component normal to the filament in the $\xi$ direction that is just inside the wake boundary and $u_{\xi_{R_0^+}}$ is that component which is just outside the wake boundary. In addition

$$\frac{u_{\xi_{R_0^-}} + u_{\xi_{R_0^+}}}{2} = w\cos\varphi_{R_0} \qquad (II-8)$$

If $\Gamma(\xi)$ is constant, then $u_{\xi_{R_o^+}}$ is zero and $u_{\xi_{R_o^-}} = 2W\cos\varphi_{R_o}$.
If $\Gamma(\xi)$ is not constant, then it may be shown that $u_{\xi_{R_o^+}}$ has a period $\frac{(V_\infty + W)\cos\varphi_{R_o}}{b\left(\frac{\Omega}{2\pi}\right)}$ and is such a function that

$$\int_{-\frac{(V_\infty+W)\cos\varphi_{R_o}}{2b\left(\frac{\Omega}{2\pi}\right)}+\xi_1}^{\frac{(V_\infty+W)\cos\varphi_{R_o}}{2b\left(\frac{\Omega}{2\pi}\right)}+\xi_1} u_{\xi_{R^+}}\, d\xi = 0 \qquad (II-9)$$

This is most easily shown by taking the line integral just outside the wake boundary along a line $\xi$ = CONSTANT where $u_\xi = 0$ and then closing the path along a line $\xi$ = CONSTANT for which $u_\xi = f(\xi)$.

Consider now the region adjacent to the line of contact of the inner helical vortex sheet with the cylindrical wake boundary sheet of helical vortex filaments as shown in figure II-4. There can be no radial velocity in the region indicated by the arrows because of the assumption that the wake boundary is a right circular cylinder. Therefore in this region $\Gamma(x)$ = CONST. and the strength of the vortex sheet is zero. The requirement on $u_\xi$ for the helical sheet filaments just inside the cylindrical wake is

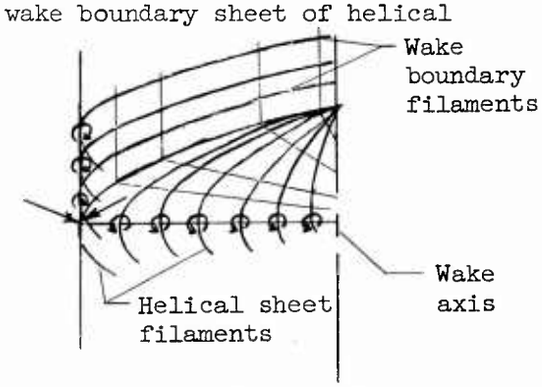


Figure II-4. Region adjacent to intersection of inner helical sheet with boundary sheet.

$$u_{\xi_{R_o^-}} = W\cos\varphi_{R_o^-} \qquad (II-10)$$

The requirement on the helical filaments of the wake boundary is

$$u_{\xi_{R_o}} = W\cos\varphi_{R_o} \qquad (II-11)$$

Thus the strength of the boundary sheet in this region must be zero because $\varphi$ is continuous and $\varphi_{R_o^-} \to \varphi_{R_o}$ AS $R_o^- \to R_o$ so that

$$\frac{u_{\xi_{R_o^-}} + u_{\xi_{R_o^+}}}{2} = \frac{W\cos\varphi_{R^-} + W\cos\varphi_{R^+}}{2} = W\cos\varphi_R \qquad (II-12)$$

and

$$\Gamma(\xi) = u_{\xi_{R_o^-}} - u_{\xi_{R_i^+}} = w\cos\varphi_{R_o^-} - w\cos\varphi_{R_o^+} = 0 \qquad (II-13)$$

Returning now to the case for which $u_{\xi_o}$ is different from zero, it will be shown that a solution may be obtained if the inner and outer sheets have different geometric pitches. From equation II-5

$$u_\xi = u_{\xi_o}\sin\varphi$$

The requirement that the inner helical sheets move as a rigid body gives

$$u_{\xi_x} = w\cos\varphi_x$$

Taking the line integral along a path $\xi = \xi_1$ ; $r = r_1$ and then closing the path along a line $\xi = \xi_1$ ; $r = r_1$

$$-\int u_\xi\, d\xi + \left[2\pi r\cos\varphi + \frac{V_\infty + w}{\left(\frac{\Omega}{2\pi}\right)}\sin\varphi\right]\left[u_{\xi_o}\sin\varphi\right] = b\,\Gamma(r)$$

For the last outboard filament in the inner helical vortex sheet

$$u_{\xi_{R_o^-}} = w\cos\varphi_{R_o^-}$$

and

$$u_{\xi_{R_o^-}} = u_{\xi_o}\sin\varphi_{R_o^-}$$

The helical filaments in the cylindrical sheet that are adjacent to the aforementioned filament have a velocity in the $\xi$ direction

$$u_{\xi_{R_o}} = \tfrac{1}{2}\left(u_{\xi_o}^2\sin^2\varphi_{R_o^-} + w^2\cos^2\varphi_{R^-}\right)^{\frac{1}{2}} \qquad (II-14)$$

and the cylindrical sheet strength at this point is

$$\Gamma(\xi)_{R_o} = \left(u_{\xi_o}^2\sin^2\varphi_{R_o^-} + w^2\cos^2\varphi_{R_o^-}\right)^{\frac{1}{2}} \qquad (II-15)$$

for zero induced velocity outside the wake at this point.

This last condition is rigorously applicable to the heavily loaded shrouded propeller in which the helical filaments of the outer boundary have a different apparent axial motion than that of the inner helical sheet. In Appendix III, this condition will be used to obtain the blade bound vortex distribution for a shrouded propeller having an infinite number of blades.

Returning to the lightly loaded case, that is, the case in which $u_{\xi_0} = 0$ and the geometric pitch of all the helical filaments is constant, it is now possible to calculate the thrust. Since the motion of each filament is normal to itself, the velocity potential is

$$\phi' = f(\xi - wt\omega z\varphi, r) \qquad (II-16)$$

so that $\phi'$ or grad $\phi'$ remains unchanged if the reference point moves such that

$$\xi = \xi_m + (w\omega z\varphi)t \quad ; \quad r = r_m$$

Therefore

$$\frac{\partial \phi'}{\partial t} = \frac{\partial \phi'}{\partial \xi}\frac{d\xi}{dt}$$

$$= -w\omega z\varphi \frac{\partial \phi'}{\partial \xi}$$

$$= -u_\xi w \omega z\varphi$$

since

$$u_\xi = \frac{\partial \phi'}{\partial \xi}$$

or for the case of the coordinates fixed in the shroud

$$\frac{\partial \phi}{\partial t} = -(V_\infty + w)u_\xi \omega z\varphi = -(V_\infty + w)u_z \qquad (II-17)$$

For the disturbed flow field, equation II-2 becomes

$$\frac{p}{\rho} + \frac{1}{2}V^2 - (V_\infty + w)u_\xi \omega z\varphi = \frac{p_0}{\rho} \qquad (II-18)$$

At each point on the wake boundary, the static pressures must be identical both inside and outside.

$$p_{R_o^-} = p_{R_o^+} \tag{II-19}$$

$$p_{o_{2_{R_o^-}}} - \tfrac{1}{2}\rho V_{R_o^-}^2 + \rho u_{s_{R_o^-}}(V_\infty + w)\cos\varphi_o = p_{o_{2_{R_o^+}}} - \tfrac{1}{2}\rho V_{R_o^+}^2 + \rho u_{s_{R_o^+}}(V_\infty + w)\cos\varphi_o \tag{II-20}$$

Outside the wake,

$$p_{o_{2_{R_o^+}}} = p_\infty + \tfrac{1}{2}\rho V_\infty^2$$

and

$$p_\infty - p = \tfrac{1}{2}\rho V^2 - \rho u_s (V_\infty + w)\cos\varphi - \tfrac{1}{2}\rho V_\infty^2 \tag{II-21}$$

Inside the wake

$$p + \tfrac{1}{2}\rho V^2 - \rho u_s (V_\infty + w)\cos\varphi = p_{o_{2_{R_o^-}}} = p_{o_1} + \left(p_{o_{2_{R_o^-}}} - p_{o_{2_{R_o^+}}}\right)$$

$$p + \tfrac{1}{2}\rho V^2 - \rho u_s \cos\varphi (V_\infty + w) = p_\infty + \tfrac{1}{2}\rho V_\infty^2 + \tfrac{1}{2}\rho V_{R_o^-}^2 - \rho u_{s_{R_o^-}} w\cos\varphi_o - \tfrac{1}{2}\rho V_{R_o^+}^2 + \rho u_{s_{R_o^+}}\cos\varphi_o (V_\infty + w)$$

$$p_\infty - p = \tfrac{1}{2}\rho\left[V^2 - V_{R_o^-}^2 + V_{R_o^+}^2 - V_\infty^2\right] - \rho(V_\infty + w)\left[u_s\cos\varphi - \left(u_{s_{R_o^-}} - u_{s_{R_o^+}}\right)\cos\varphi_o\right] \tag{II-22}$$

Equation II-1 then becomes

$$T = \frac{b\Omega\rho}{2\pi(V_\infty + w)}\int_{\text{VOLUME INSIDE WAKE}}\Big\{V_\infty u_s\cos\varphi + u_s^2\cos^2\varphi + \tfrac{1}{2}\left(V_{R_o^-}^2 + V_\infty^2 - V^2 - V_{R_o^+}^2\right) - (V_\infty + w)\left(u_{s_{R_o^-}}\cos\varphi_o - u_{s_{R_o^+}}\cos\varphi_o - u_s\cos\varphi\right)\Big\}\, dz\, dS$$

$$+ \frac{b\Omega\rho}{2\pi(V_\infty + w)}\int_{\text{VOLUME OUTSIDE WAKE}}\Big\{V_\infty u_s\cos\varphi + u_s^2\cos^2\varphi + \tfrac{1}{2}\left(V_\infty^2 - V^2\right) + u_s\cos\varphi\,(V_\infty + w)\Big\}\, dz\, dS \tag{II-23}$$

where the integration extends over a volume equal to the product of the control surface area normal to the wake axis at a far distance behind the shrouded propeller and the distance between successive vortex sheets.

Consider the line integral along the closed path $\overline{ABCDA}$ inside the wake as shown in figure II-5. The lines $\overline{AB}$ and $\overline{CD}$ are radial lines lying on the surface of the helical vortex sheet, $\overline{BC}$ coincides with the axis of the wake and $\overline{DA}$ is parallel to the wake axis.

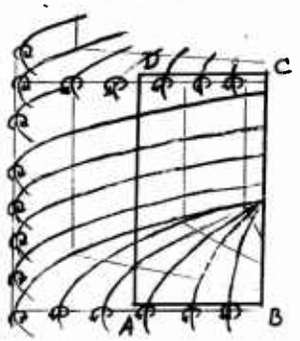


Figure II-5. Path of integration within wake.

$$\int_A^B u_r\,dr + \int_B^C u_{\xi_0}\,dz + \int_C^D u_r\,dr + \int_D^A u_z\,dz = \Gamma(x)$$

or since

$$u_{\xi_0} = 0 \qquad \text{AND} \qquad \int_A^B u_r\,dr + \int_C^D u_r\,dr = 0$$

$$\int_D^A u_z\,dz = \Gamma(x)$$

or $$\int_D^A u_\xi \cos\varphi\,dz = \Gamma(x)$$

Similarly along a path outside the wake

$$\int u_\xi \cos\varphi\,dz = 0$$

Thus

$$\frac{b\Omega\rho}{2\pi(V_\infty+w)}\int_{\text{VOLUME INSIDE WAKE}}(2V_\infty+w)\,u_\xi\cos\varphi\,dz\,dS = w(2V_\infty+w)\rho\int_0^{2\pi}\int_0^{R_0}K(x)\,r\,dr\,d\theta$$

$$= \rho w(2V_\infty+w)R^2\int_0^1\int_0^{2\pi}K(x)\,x\,dx\,d\theta$$

$$= \rho(2V_\infty+w)\mu w F \qquad \text{(II-24)}$$

where F the cross-sectional area of the ultimate wake

$$\mu \equiv 2\int_0^1 K(x)\, x\, dx \qquad (II-25)$$

$$K(x) \equiv \frac{\Gamma(x)}{\left(\frac{2\pi(V_\infty+w)w}{b\Omega}\right)} \qquad (II-26)$$

Consider the remaining integrals term by term.

$$-\frac{b\Omega\rho}{2\pi(V_\infty+w)}\int_{\text{VOLUME INSIDE WAKE}}(V_\infty+w)\cos\varphi_0\left(u_{s_{R_0^-}}-u_{s_{R_0^+}}\right)dz\,dS = -\frac{b\Omega\rho}{2\pi(V_\infty+w)}(V_\infty+w)\int_0^{R_0}\int_0^{2\pi}\Gamma(1)\,r\,dr\,d\theta$$

$$= -\rho(V_\infty+w)w\,K(1)R^2\int_0^1\int_0^{2\pi} x\,dx\,d\theta$$

$$= -\rho(V_\infty+w)w\,(2\pi R^2)\left(\tfrac{1}{2}\right)K(1)$$

$$= -\rho(V_\infty+w)w\,K(1)\,\mathcal{F} \qquad (II-27)$$

where $K(1)$ is $K(x)$ evaluated at $x = 1.0$.

For the third term in the first integral of equation II-23

$$V_{R_0^-}^2 = \left(V_\infty + u_{s_{R_0^-}}\cos\varphi_0\right)^2 + u_{s_{R_0^-}}^2\sin^2\varphi_0 = V_\infty^2 + 2V_\infty u_{s_{R_0^-}}\cos\varphi_0 + u_{s_{R_0^-}}^2$$

$$V_{R_0^+}^2 = \left(V_\infty + u_{s_{R_0^+}}\cos\varphi_0\right)^2 + u_{s_{R_0^+}}^2\sin^2\varphi_0 = V_\infty^2 + 2V_\infty u_{s_{R_0^+}}\cos\varphi_0 + u_{s_{R_0^+}}^2$$

$$V^2 = \left(V_\infty + u_s\cos\varphi\right)^2 + u_s^2\sin^2\varphi + u_r^2 = V_\infty^2 + 2V_\infty u_s\cos\varphi + u_s^2 + u_r^2$$

so that

$$\tfrac{1}{2}\left(V_{R_0^-}^2 + V_\infty^2 - V^2 - V_{R_0^+}^2\right) = V_\infty \cos\varphi_0 \left(u_{s_{R_0^-}} - u_{s_{R_0^+}}\right) - V_\infty u_s \cos\varphi + \tfrac{1}{2}\left(u_{s_{R_0^-}}^2 - u_{s_{R_0^+}}^2\right)$$

$$- \tfrac{1}{2}\left(u_s^2 + u_r^2\right) \qquad \text{(II-28)}$$

The first term of equation II-28 is upon comparison with equation II-27

$$\frac{b\Omega\rho}{2\pi(V_\infty + w)} \int_{\text{VOLUME INSIDE WAKE}} V_\infty \cos\varphi_0 \left(u_{s_{R_0^-}} - u_{s_{R_0^+}}\right) dz\, dS = \rho V_\infty w K(1) F \qquad \text{(II-29)}$$

The second term is upon comparison with equation II-24

$$-\frac{b\Omega\rho}{2\pi(V_\infty + w)} \int_{\text{VOLUME INSIDE WAKE}} V_\infty u_s \cos\varphi\, dz\, dS = -\rho V_\infty w \mu F \qquad \text{(II-30)}$$

The third term may be reduced to

$$\tfrac{1}{2}\left(u_{s_{R_0^-}}^2 - u_{s_{R_0^+}}^2\right) = \tfrac{1}{2}\left(u_{s_{R_0^-}} + u_{s_{R_0^+}}\right)\left(u_{s_{R_0^-}} - u_{s_{R_0^+}}\right)$$

$$= w \cos\varphi_0 \left(u_{s_{R_0^-}} - u_{s_{R_0^+}}\right)$$

which on comparison with equation II-27

$$\frac{b\Omega\rho}{2\pi(V_\infty + w)} \int_{\text{VOLUME INSIDE WAKE}} w \cos\varphi_0 \left(u_{s_{R_0^-}} - u_{s_{R_0^+}}\right) dz\, dS = \rho w^2 K(1) F \qquad \text{(II-31)}$$

The remaining terms in equation II-28 are

$$-\frac{b\Omega\rho}{2\pi(V_\infty + w)} \int_{\text{VOLUME INSIDE WAKE}} \tfrac{1}{2}\left(u_r^2 + u_s^2\right) dz\, dS \qquad \text{(II-32)}$$

where it is remembered that the volume is enclosed between two parallel planes which are normal to the wake axis and are a distance apart equal to the distance between two successive helical vortex sheets. This

volume is also equal to that enclosed between a full turn of two successive helical sheets so that, on account of helical symmetry, the integral may be written

$$-\frac{b\Omega\rho}{2\pi(V_\infty+w)}\int_{VOL}\tfrac{1}{2}\nabla\phi'\cdot\nabla\phi'\,d\xi\,dS' \qquad (II-33)$$

where $dS'$ an element of area of the vortex sheet

$\phi'$ the disturbance velocity potential

Using Green's first identity or theorem

$$\int_{VOL}\nabla\phi'\cdot\nabla\phi'\,d\xi\,dS' = \int_{SURFACE}\omega_x\varphi\,(\phi'\nabla\phi')\cdot d\bar{S}' \qquad (II-34)$$

where $d\bar{S}'$ is an element of vector area of the vortex sheet and $\phi'$ and $\nabla\phi'$ are evaluated at the vortex sheet. The vector $d\bar{S}'$ is outwardly directed with respect to the volume. For corresponding elemental areas on successive vortex sheets enclosing the volume, $d\bar{S}'$ has opposite signs while $\nabla\phi'$ must have the same sign to satisfy the required motion of the vortex sheet. Since the integrand of equation II-32 must be positive, the smaller value of $\phi'$ goes with the elemental area vector which has the negative sign. If $\phi'$ is replaced by $\Delta\phi'$ then the integration need be carried out over one of the surfaces, where $\Delta\phi'$ is the difference in potential between corresponding elemental areas of the vortex sheet. There is no contribution from the boundary sheet because the vector area and velocity vector are perpendicular.

At the vortex sheet $\nabla\phi' = w\cos\varphi$ and $\Delta\phi' = \Gamma(x)$ so that equation II-32 becomes

$$w\int_{SURFACE}\Gamma(x)\cos\varphi\,dS' = w\int_{SURFACE}\Gamma(x)\,dS$$

$$= w\int_0^{R_0}\int_0^{2\pi}\Gamma(x)\,r\,dr\,d\theta$$

and finally

$$-\frac{b\Omega\rho}{2\pi(V_\infty+w)}\int_{\text{VOLUME INSIDE WAKE}}\tfrac{1}{2}\left(u_r^2+u_s^2\right)dz\,dS=-\tfrac{1}{2}w^2\mu\rho F \qquad (II-35)$$

For the second term in both integrands of equation II-23 define a quantity as was done by Theodosen in reference 3, such that

$$\frac{b\Omega\rho}{2\pi(V_\infty+w)}\int u_s^2\omega^2\varphi\,dz\,dS=\rho\epsilon w^2F \qquad (II-36)$$

where $\epsilon$ may be termed the axial energy loss factor. The remaining term in the third term in the second integral of equation II-23. Expanding this term

$$\tfrac{1}{2}\left(V_\infty^2-v^2\right)=\tfrac{1}{2}\left[V_\infty^2-\left(V_\infty+u_s\omega\varphi\right)^2-u_s^2\sin^2\varphi-u_r^2\right]$$

$$=-V_\infty u_s\omega\varphi-\tfrac{1}{2}\left(u_r^2+u_s^2\right)$$

The integral of the first term is zero because $\int_{z_1}^{z_2}u_s\omega\varphi\,dz$ is zero over the axial distance considered. The second term is

$$-\frac{b\Omega\rho}{2\pi(V_\infty+w)}\int_{\text{VOLUME OUTSIDE WAKE}}\tfrac{1}{2}\left(u_r^2+u_s^2\right)dz\,dS=-\tfrac{1}{2}\,\frac{b\Omega\rho}{2\pi(V_\infty+w)}\int\nabla\phi'\cdot\nabla\phi'\,dz\,dS$$

which by Green's first identity is

$$-\tfrac{1}{2}\,\frac{b\Omega\rho}{2\pi(V_\infty+w)}\int\left(\phi'\nabla\phi'\right)\cdot d\bar{S}'$$

where $d\bar{S}'$ is a element of area enclosing the volume. At the outer cylindrical boundary (i.e. $r=\infty$) $\nabla\phi'$ is zero. At the inner cylindrical boundary (i.e. $r=R_o$), $\nabla\phi'$ is perpendicular to $d\bar{S}'$ so that $\phi'\nabla\phi'\cdot d\bar{S}'$ is zero. In the general case and for the remaining area, it appears that

no additional simplifications can be made except to introduce another "loss factor" as was done in equation II-34 . However, for the optimum condition of the lightly loaded shrouded propeller, there should be no disturbance velocities outside of the wake. In this instance, the thrust becomes

$$T = \rho F \left\{ (2V_\infty + w) w \varkappa - (V_\infty + w) w K(1) + V_\infty w K(1) - V_\infty w \varkappa \right.$$
$$\left. + w^2 K(1) - \tfrac{1}{2} w^2 \varkappa + \epsilon w^2 \right\}$$

or $$T = \rho F \left\{ (V_\infty + \tfrac{1}{2} w) w \varkappa + \epsilon w^2 \right\} \qquad (II-37)$$

Defining a nondimensional thrust coefficient

$$C_S = \frac{T}{\frac{1}{2} \rho V_\infty^2 F} = 2 \varkappa \overline{w} \left\{ 1 + \overline{w} \left( \tfrac{1}{2} + \frac{\epsilon}{\varkappa} \right) \right\} \qquad (II-38)$$

which is identical in form with the thrust coefficient of equation 31 , Chapter IV of reference 3.

The induced energy loss per unit time in the wake is found by the methods of classical mechanics by integrating with respect to time $d\tau = \frac{dz}{V_\infty + w}$ and averaging over a time $\Delta\tau = 2\pi/b\Omega$ for the lightly loaded shrouded propeller wake for which there are no disturbance velocities outside the wake. Thus

$$E = \frac{b\Omega}{2\pi} \iiint \left[ \left( p' - p_\infty + \tfrac{1}{2} \rho v^2 \right) u_z + \tfrac{1}{2} \rho v^2 V_\infty \right] d\tau \, dS \qquad (II-39)$$

where this equation is written with respect to an axis system fixed in space and where

$p'$ static pressure in disturbed region

$p_\infty$ static pressure in undisturbed region

$v$ total induced velocity.

Equation II-18 becomes with respect to fixed spatial coordination

$$p' - p_\infty + \tfrac{1}{2}\rho v^2 = \rho w u_z \qquad \text{(II-40)}$$

so that upon substitution into equation II-39

$$E = \frac{b\Omega\rho}{2\pi(V_\infty + w)} \iiint \left[ w u_z^2 + \tfrac{1}{2} v^2 V_\infty \right] dz\, dS$$

Comparing this integral with the integrals of equations II-35 and II-36 it may be seen that

$$E = \rho \varkappa w^2 F \left( \frac{V_\infty}{2} + \frac{\epsilon}{\varkappa} w \right) \qquad \text{(II-41)}$$

or in nondimensional coefficient form

$$e = \frac{E}{\frac{1}{2}\rho V_\infty^2 F V_\infty} = 2\varkappa \bar{w}^2 \left( \tfrac{1}{2} + \frac{\epsilon}{\varkappa} \bar{w} \right) \qquad \text{(II-42)}$$

which is identical in form with equation 36 in Chapter IV of reference 3.

The total power coefficient $c_p$ is found by adding equations II-38 and II-42 .

$$c_p = 2\varkappa \bar{w} (1 + \bar{w}) \left( 1 + \frac{\epsilon}{\varkappa} \bar{w} \right) \qquad \text{(II-43)}$$

The ideal propeller efficiency $\eta_i$ is then

$$\eta_i = \frac{c_s}{c_p} = \frac{1 + \bar{w} \left( \frac{1}{2} + \frac{\epsilon}{\varkappa} \right)}{(1 + \bar{w}) \left( 1 + \frac{\epsilon}{\varkappa} \right)} \qquad \text{(II-44)}$$

Although the results of this analysis are identical with those of reference 3, it is to be noted that the values of the quantities $\epsilon$ and $\varkappa$ for the shrouded propeller will be appreciably different from those values for the free propeller. However, the methods for evaluating $\epsilon$ and $\varkappa$ will be identical in form with the results of this reference.

The total velocity loss factor $\varkappa$ is found by definition from equation II-25 The axial loss factor $\epsilon$ is determined by equation 59 of Chapter IV of reference 3 where it is shown that

$$\epsilon = \varkappa + \tfrac{1}{2}\lambda \frac{d\varkappa}{d\lambda} \qquad \text{(II-45)}$$

The total velocity loss factor $\varkappa$ must of course be a function of number of blades and wake geometric pitch angle or $\lambda$ and is to be determined from a series of experiments or by a numerical analysis.

These quantities may be evaluated for the infinite number of blades cases of the heavily-loaded shrouded propeller and the heavily loaded free propeller. Making use of equation III-8 from Appendix III,

$$\varkappa = 2\int_0^1 K(x)\, x\, dx$$

$$= \left[1 - \lambda^2 \ln\left(1+\frac{1}{\lambda^2}\right)\right]\left[1 - \frac{3}{16}\overline{w}\,\frac{\lambda^2+2}{\lambda^2(\lambda^2+1)}\right] \qquad \text{(II-46)}$$

Substituting this value of $\varkappa$ into equation II-45 yields

$$\epsilon = 1 + \frac{\lambda^2}{\lambda^2+1} - 2\lambda^2 \ln\left(1+\frac{1}{\lambda^2}\right)$$

$$-\frac{3}{16}\overline{w}\left[1-\lambda^2\ln\left(1+\frac{1}{\lambda^2}\right)\right]\left[\frac{\lambda^4+2\lambda^2+2}{\lambda^2(\lambda^2+1)^2}\right] \qquad \text{(II-47)}$$

## APPENDIX III

## DETERMINATION OF THE OPTIMUM LOADING FOR A HEAVILY LOADED PROPELLER HAVING AN INFINITE NUMBER OF BLADES

One of the cases considered in Appendix II was that in which the inner helical vortex sheet had a different geometric pitch from the outer wake boundary vortex sheet. Such an occurance is easier to visualize for the case of an infinite number of blades because the outer vortex filaments must form a right circular cylindrical surface of constant filament density (i.e. sheet strength) and the pitch angle of these filaments must be the same everywhere on this surface. As a result, the outer vortex filaments will have a different apparent axial motion than that of the inner helical sheet. For a shrouded propeller with a finite number of blades, the outer boundary may again be a right circular cylinder or the geometry may be complicated by the presence of scallops in the boundary sheet. In either event, it is possible for the pitch angle of these outer filaments to vary with distance along the filaments, and also, for the pitch angle to vary with time with respect to an axis system attached to a particular element of the filament, while the overall boundary pattern appears to remain fixed with respect to the inner helical sheet. In such an instance, however, it is easily seen that all of the vortex filaments must be of constant strength although the local filament density or sheet strength may vary. In any case, the only real requirement is that the boundary sheet distribution and geometry appear invariant with respect to the inner helical vortex sheet.

For the infinite number of blades case, the theoretical blade bound vortex distribution may be determined because the wake geometry is known and the induced velocity field outside the wake system is zero. From equation II-14

$$u_{\zeta_R} = \tfrac{1}{2}\left(u_{\zeta_0}^2 \sin^2\varphi_{R-} + w^2\cos^2\varphi_{R-}\right)^{\frac{1}{2}}$$

which is the total induced velocity vector and is of necessity, mutually

perpendicular to the boundary filaments and the radial coordinate. The velocity diagrams for the outer most filament of the inner sheet and the adjacent boundary filament are given in figure III-1.

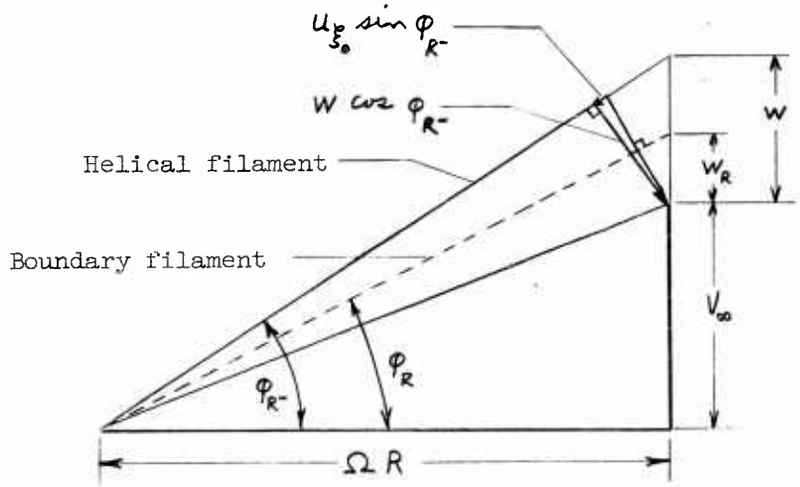


Figure III-1. Velocity diagram for outermost filament of inner vortex sheet and the adjacent boundary filament.

From figure III-1

$$w_R = \frac{1}{2}\left[w^2\cos^2\varphi_{R-} + u_{\xi_0}^2 \sin^2\varphi_{R-}\right]^{\frac{1}{2}} \sec\left\{\varphi_{R-} - \arccos \frac{w\cos\varphi_{R-}}{\left[w^2\cos^2\varphi_{R-} + u_{\xi_0}^2\sin^2\varphi_{R-}\right]^{\frac{1}{2}}}\right\}$$

or after simplifying and arranging terms,

$$w_R = \frac{1}{2}\left\{\frac{w^2\cos^2\varphi_{R-} + u_{\xi_0}^2 \sin^2\varphi_{R-}}{w\cos^2\varphi_{R-} + u_{\xi_0}\sin^2\varphi_{R-}}\right\} \qquad \text{(III-1)}$$

A second relation may be obtained by considering the line integral enclosing a portion of the wake boundary filaments as shown in figure III-2. In this figure, a section of the cylindrical wake boundary equal in length to the geometric pitch has been unwrapped and presented in a true perspective. Thus the line $\overline{CD}$ represents the continuation of one of the outermost filaments $\overline{AB}$ of the inner sheet. The dashed lines represent the boundary filaments.

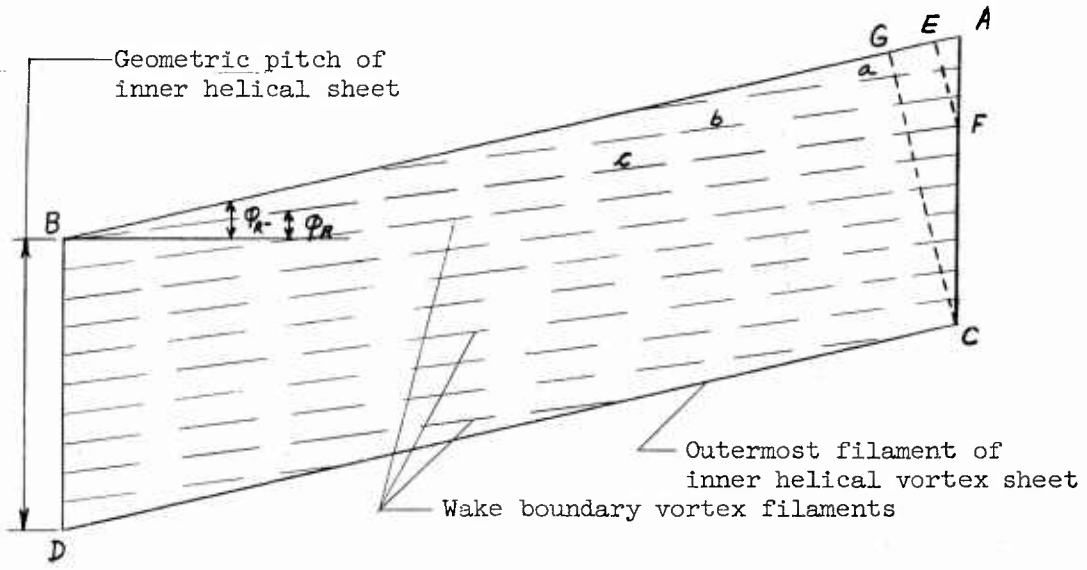


Figure III-2. Relationship of boundary filaments to inner helical sheet filaments.

The first line integral is taken along the inner filament $\overline{AB}$, along which the velocity component is $u_{\xi_0} \sin \varphi_{R-}$ through the boundary sheet at $B$, back along a path outside the wake parallel to $\overline{AB}$ when the induced velocity components are zero; and is closed at $A$; thereby enclosing the boundary filaments "a" through "c". A second line integral is taken inside the wake boundary adjacent to the boundary filaments along the line $\overline{EF}$ where the velocity component is $w \cos \varphi_{R-}$, through the boundary sheet at $F$, back along a path outside the wake parallel to $\overline{FE}$ where the induced velocity components are zero, and is closed through the boundary sheet at $E$; thereby enclosing the same filaments as before. The line integrals around these two paths are identical so that

$$(\overline{EB}) \tan(\varphi_{R-} - \varphi_R) w \cos \varphi_{R-} = (\overline{EB}) u_{\xi_0} \sin \varphi_{R-}$$

or from figure III-1

$$\left\{ \frac{\frac{V_\infty + w}{\Omega R_0} - \frac{V_\infty + W_R}{\Omega R_0}}{1 + \left(\frac{V_\infty + w}{\Omega R_0}\right)\left(\frac{V_\infty + W_R}{\Omega R_0}\right)} \right\} w \cos \varphi_{R-} = u_{\xi_0} \sin \varphi_{R-}$$

Simplifying yields

$$u_{\xi_0} \sin \varphi_{R-} = \frac{(W - W_R) W \Omega R_0 \cos \varphi_{R-}}{\Omega R_0^2 + (V_\infty + W)(V_\infty + W_R)} \qquad (III-2)$$

Combining equations III-1 and III-2 and dividing by $V_\infty$ yields the cubic equation

$$u_{\xi_0}^3 \sin^3 \varphi_{R-} + 2 \csc \varphi_{R-} \left[1 + \tfrac{3}{2} \bar{w} \cos^2 \varphi_{R-}\right] \bar{u}_{\xi_0}^2 \sin^2 \varphi_{R-}$$

$$+ 2 \bar{w} \cot^2 \varphi_{R-} \left[1 + \bar{w} \left(1 - \tfrac{3}{2} \sin^2 \varphi_{R-}\right)\right] \bar{u}_{\xi_0} \sin \varphi_{R-}$$

$$- \bar{w}^3 \cot \varphi_{R-} \cos^3 \varphi_{R-} = 0 \qquad (III-3)$$

where $\bar{u}_{\xi_0} = u_{\xi_0}/V_\infty$ ; $\bar{w} = w/V_\infty$

This may be reduced in the usual manner to

$$X^3 - \tfrac{1}{3} \csc^2 \varphi_{R-} \left[4 + 6 \bar{w} \cos^2 \varphi_{R-} + 3 \bar{w}^2 \cos^2 \varphi_{R-}\right] X$$

$$+ \tfrac{2}{27} \csc^3 \varphi_{R-} \left[8 + 18 \bar{w} \cos^2 \varphi_{R-} + 9 \bar{w}^2 \cos^2 \varphi_{R-}\right] = 0 \qquad (III-4)$$

where $X = \bar{u}_{\xi_0} \sin \varphi_{R-} + \tfrac{2}{3} \csc \varphi_{R-} \left[1 + \tfrac{3}{2} \bar{w} \cos^2 \varphi_{R-}\right]$

The discriminant of the coefficients is negative so that there are three real and unequal roots. It may be shown that only one of the roots is positive and this is the desired root. Writing equation III-3 in the form

$$y^3 + p y^2 + q y + r = 0$$

and equation III-4 in the form

$$X^3 + a X + b = 0$$

the desired root is

$$\bar{u}_{\xi_0} \sin \varphi_{R-} = 2 \sqrt{\left(-\tfrac{a}{3}\right)} \cos A - \tfrac{p}{3}$$

where

$$\cos 3A = -\frac{b}{2}\sqrt{\left(-\frac{3}{a}\right)^3}$$

or upon substituting for $a$, $b$, & $p$ and neglecting terms of order $\bar{w}^3 \cos^4 \varphi_{R-}$, it is found that

$$\bar{u}_{\xi_0} \sin \varphi_{R-} \approx \frac{3}{16} \bar{w}^2 \cos^2 \varphi_{R-} \csc \varphi_{R-} \left(1 + \cos^2 \varphi_{R-}\right) \qquad \text{(III-5)}$$

or

$$u_{\xi_0} = \frac{3}{16} w \bar{w} \cot^2 \varphi_{R-} \left(1 + \cos^2 \varphi_{R-}\right) \qquad \text{(III-6)}$$

The expression for the nondimensional blade bound vortex distribution may be obtained by taking the line integral along the path $r = r_1$ ; $\zeta = \zeta_1$ on the upper surface of one of the inner vortex sheets and closing the path along a coordinate $r = r_1$ ; $\xi = \xi_1$, thereby returning to the starting point and enclosing all the inner filaments lying inboard of $r = r_1$. The velocity component along the path $r = r_1$ ; $\zeta = \zeta_1$ is $u_{\xi_0} \sin \varphi$ and the length of the path is $H \cos \varphi \cot \varphi$ where $H$ is the geometric pitch. The velocity component along the path $r = r_1$ ; $\xi = \xi_1$ is $w \cos \varphi$ and the length is $H \cos \varphi$. Thus

$$b\,\Gamma(r) = w \cos \varphi \left(H \cos \varphi\right) - u_{\xi_0} \sin \varphi \left(H \cos \varphi \cot \varphi\right) \qquad \text{(III-7)}$$

or since $K(x) = \dfrac{b\,\Gamma(r)}{H w}$

$$K(x) = \cos^2 \varphi \left[1 - \frac{3}{16} \bar{w} \cot^2 \varphi_{R-} \left(1 + \cos^2 \varphi_{R-}\right)\right]$$

But

$$\cos^2 \varphi = \frac{x^2}{x^2 + \lambda^2}$$

where

$$\lambda = \frac{V_\infty + w}{\Omega R_0}$$

so that

$$K(x) = \frac{x^2}{x^2+\lambda^2}\left\{1 - \frac{3}{16}\,\overline{w}\,\frac{\lambda^2+2}{\lambda^2(\lambda^2+1)}\right\} \qquad (III-8)$$

which represents the nondimensional blade bound vortex distribution for a heavily loaded shrouded propeller or a heavily loaded free propeller having an infinite number of blades. It is to be noted that if $\overline{w} = 0$ then the result is identical with that for the lightly-loaded infinitely bladed free propeller as given in reference 3.

APPENDIX IV

# OUTLINE OF DESIGN PROCEDURES FOR SHROUDED PROPELLERS

by

Walter Castles, Jr. and Robin B. Gray

The design of an optimum shrouded propeller follows closely the design of the optimum free propeller as given in reference 3 except that the effect of the shroud must be taken into account. In the following outline, it is assumed that the propeller is lightly loaded, that the wake vortex system has reached its ultimate configuration at the shroud trailing edge, and that the flight velocity, propeller angular velocity, number of blades, and the shroud trailing edge diameter are known.

## I. Calculation of Total Power Coefficient

Calculate the total power coefficient, $C_{P_T}$

$$C_{P_T} = \frac{\text{Shaft power available}}{\frac{1}{2}\rho V_\infty^3 F} \qquad (IV-1)$$

## II. Determination of Parameter, $w$

Find $\overline{w}$ by a trial and error solution of

$$C_{P_T} \approx C_p = 2\varkappa\overline{w}(1+\overline{w})\left(1+\frac{\epsilon}{\varkappa}\overline{w}\right) \qquad (IV-2)$$

by assuming several values of $\overline{w}$ ; calculating $\lambda$ for each $\overline{w}$ ; reading $\varkappa$ and $\frac{\epsilon}{\varkappa}$ from the charts for the proper number of blades and the calculated $\lambda$ ; and substituting these values into equation IV-2 to calculate $C_{P_T}$ . Plot these results versus $\overline{w}$ . The desired $\overline{w}$ is read off the resulting curve at the point where the curve intersects the $C_{P_T}$ value determined from equation IV-1 . (Note: It is of course assumed that the charts of $\varkappa$ versus $\lambda$ and $\frac{\epsilon}{\varkappa}$ versus $\lambda$ are available for the given number of blades. Actually the determination of the necessary charts would require an extension of the existing work to cover a range of $\lambda$'s and numbers of blades.) The value of $\overline{w}$

should be checked by redetermining $\lambda$ , $\mu$ , $\frac{\epsilon}{\mu}$ and inserting these values into equation IV-2.

III. Determination of Shroud Mean Camber Surface

A. A compatible shroud must now be designed. As mentioned in the previous appendices, the flow field about the shroud is unsteady with respect to the shroud because of the presence of the propeller having a finite number of blades. In order to obtain a shroud design, the actual wake system will be replaced with an idealized wake which will yield a steady flow field approximately equal to the time average flow of the actual unsteady field. For purposes of the outline, it is assumed that the wake boundary sheet is uniform in strength, being composed of vortex ring filaments. (Actually the inner helical vortex sheet could also be approximated by a number of uniform, coaxial vortex cylinders but for the purposes of this outline, its effects will be neglected.) The shroud design will thus be based on the mean or average velocity field. The mean axial velocity in the wake may be found by considering the physical interpretation of the mass coefficient $\mu$ . As pointed out in reference 3, the propeller imparts the full interference velocity $w$ to a column of air whose cross section is $\mu F$ . Another interpretation is obtained by considering $\mu$ to be the ratio of the mean rearward velocity $v_z$ taken over the entire wake cross section to the apparent rearward displacement velocity $w$ . Therefore

$$v_z = w\mu \qquad (IV-3)$$

B. Instead of considering the idealized wake boundary to be a uniform cylinder of vorticity, it will be more convenient to replace it with its equivalent: a uniform distribution of sinks over the area enclosed by the shroud trailing edge. The required unit sink strength of this distribution is determined from the vortex sheet strength of the assumed uniform wake boundary cylinder of vorticity. The sheet strength, itself, is equal to the change in the axial velocity component across the sheet. In this idealized case, the sheet strength per unit length $\gamma$ is equal to $v_z$ since there

are no disturbance velocities outside of the assumed vortex cylinder. Thus the required unit sink strength is

$$V_w = \frac{\gamma}{2} = \frac{v_z}{2} = \frac{1}{2}\mu w \qquad (IV-4)$$

The average total quantity or volume of flow per unit time expressed in terms of the total stream function $\Psi_{T.E.}$ is

$$\Psi_{T.E.} = (V_\infty + \mu w)F \qquad (IV-5)$$

At the shroud trailing edge, the volume of flow due to the free stream and the uniform distribution of sinks is

$$\Psi_{V_\infty} + \Psi_w = (V_\infty + \tfrac{1}{2}\mu w)F \qquad (IV-6)$$

so that the shroud must supply the remainder,

$$\Psi_s = \tfrac{1}{2} v_z F = \tfrac{1}{2}\mu w F \qquad (IV-7)$$

C. The shroud mean camber surface may now be determined as follows:

(1) Compute $\Psi_{V_\infty}$ for the field from the equation

$$\Psi_{V_\infty} = \pi r^2 V_\infty \qquad (IV-8)$$

(2) Compute $\Psi_w$ for the uniform sink strength distribution from the following equations for a number of calculating points ( $r$, $z$ ) making use of values of $\Psi_w^*$ given in Table 17 of reference 6. For computation purposes the field is divided into two regions, that part outside of the wake and that part within the wake, as the calculation of $\Psi_w$ will depend on the location of the calculating point in addition to its coordinates. It is also noted that the flow is axially symmetric so that the stream lines need only be determined in a radial plane.

(a) For points in the flow ahead of the shroud trailing edge location

$$\Psi_w = \mu w R_o^2 \Psi_w^* \qquad (IV-9)$$

(b) For points in the flow field downstream of the shroud trailing edge and outside the wake

$$\Psi_w = \mu w R_o^2 (\pi - \Psi_w^*) \qquad (IV-10)$$

(c) For points in the flow field downstream of the shroud trailing edge and inside the wake

$$\Psi_w = \mu w (\pi r^2 - R_o^2 \Psi_w^*) \qquad (IV-11)$$

(3) If the shroud has a center body, the stream function for the singularity distribution describing its shape may be determined by various readily available methods as in Reference 7. In most cases a simple source-sink distribution may be sufficiently accurate.

(4) Assume a length for the shroud and, in addition, assume a bound vortex strength distribution to be placed along the shroud mean camber line. The only initial requirement on this bound vortex distribution is that it be equal to the assumed wake boundary sheet strength at the shroud trailing edge so that the flow will be tangent to the shroud mean camber line at this point, i.e. there will be no discontinuity in streamline slope at the trailing edge. Linear variations in the distribution are sufficiently accurate for this analysis. Further approximate this bound vortex sheet distribution with a number of finite strength vortices whose strengths are proportional to the area under the curve as shown in Figure IV-1.

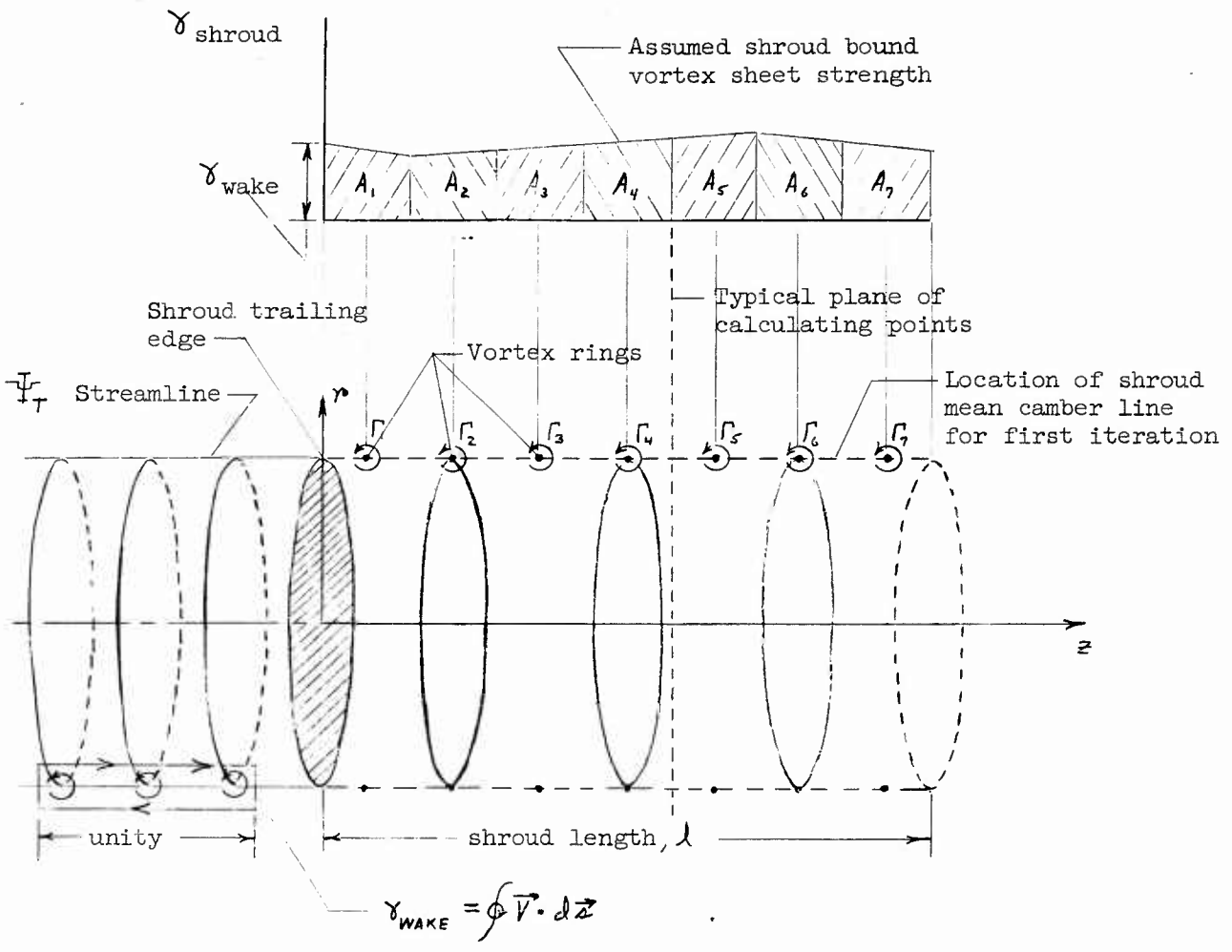


Figure IV-1. Vortex pattern used in shroud design.

Then

$$\left.\begin{aligned} \Gamma_1 &= k A_1 \\ \Gamma_2 &= k A_2 \\ &\vdots \\ \Gamma_m &= k A_m \end{aligned}\right\} \quad (IV-12)$$

These finite vortices are placed for the first iteration on the surface of a right circular cylinder whose radius is equal to the radius of the wake. The nondimensional stream function $\Psi_S^*$ at point $(r, z)$ for a vortex ring at point $(r', 0)$ for the assumed geometry may be read from Table 3 of reference 6 or from a plot of Table 3 where the $z$-coordinate of this paper corresponds to the $x$-coordinate of the table.

$$\Psi_{S_{T.E.}} = \frac{k r'}{2\pi} \Psi^*_{S_{(r', z')}} \quad (IV-13)$$

where $\Psi_S^*$ is identical with $\Psi_\gamma^*$ of the table.

The value of "k" which satisfies the volume flow through the trailing edge disk area may be found from the relation

$$\Psi_S = \sum_{m=1}^{m} \Psi_{S_{T.E.(r', z')}} \quad (IV-14)$$

or from equation IV-7 and IV-13

$$\tfrac{1}{2} u w F = \sum_{m=1}^{\infty} \frac{k r'}{2\pi} \Psi_S^* \quad (IV-15)$$

(5) For the same calculating points $(r, z)$ used in section C-1, C-2, and C-3 compute the contribution to the total stream function of the shroud vortex sheet by the following relation

$$\Psi_{S_{(r, z)}} = \frac{k r'}{2\pi} \Psi^*_{S_{(r', z')}} \quad (IV-16)$$

(Note: The vortex rings should be located in the midplanes of the calculating points as shown in figure IV-1 .)

(6) Find $\Psi_T$ for all the calculating points by adding the contributions from sections C-1, C-2, C-3, and C-5. From a cross-plot determine the line along which $\Psi_T = \Psi_{T.E.}$. This line is the new position of the shroud mean camber surface. If the shape is undesirable from a physical or common sense viewpoint, i.e. results in such a large expansion angle that the adverse pressure gradient forces flow separation, or results in a reflex camber surface, the assumed bound vortex strength must be adjusted. The location of the mean camber surface may be displaced radially at a given longitudinal position by increasing the local bound vortex strength for the next iteration, or vice versa. It should be noted that the shroud thickness distribution may account for all of the allowable trailing edge expansion angle. If the shroud mean camber surface has too much curvature, the shroud must be lengthened and vice versa.

(7) For the next iteration, the shroud bound vortex rings are moved to the surface determined in section C-6 and the process is repeated from section C-4 until a satisfactory mean camber surface is established.

## IV. Shroud Thickness Distribution

The following method appears to yield a reasonable shroud thickness distribution without an unreasonable amount of work.

A. Construct a reasonable inner contour using elements of existing airfoil sections being careful to match slopes and radii of curvature insofar as possible where different airfoil sections are joined.

B. Equidistant on either side of and very close to the mean camber surface determined in section 5, place a pair of vortex rings of equal strength but opposite sign as shown in figure IV-2. The location of these vortices must be well within the thickness distribution. Using the stream function data from table 3 reference 6, determine the strength of the vortex rings which will locally, i.e. in the plane of the rings, move the $\Psi_T$ streamline radially inward to the assumed inner shroud contour.

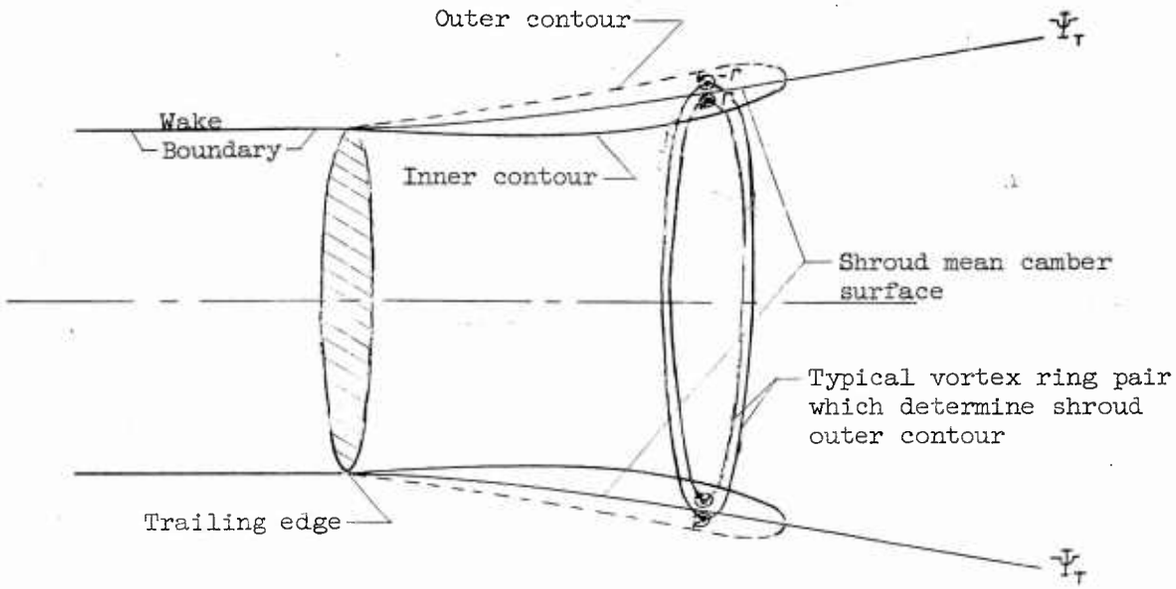


Figure IV-2. Location of vortex rings for determination of outer shroud contour

C. A corresponding outer point may now be determined in the plane of the ring pair by adding the stream function due to the ring pair to the existing values of the stream function outside of the mean camber surface. The desired point is obtained at that radius where $\Psi$ again is equal to $\Psi_T$ . It is noted that this method is approximate and does not furnish a solution for the shroud pressure distribution. The outer contour is found by connecting a sufficient number of points so determined with a smooth curve.

V. Propeller Design

A. Determine the induced axial inflow velocity distribution $\mu_p$ at the propeller plane due to the various assumed singularity distributions. This may be found from the stream functions previously determined or from the appropriate tables of reference 6. From this fictitious axial induced inflow distribution $\mu_p$ substract $\frac{1}{2}\nu_z = \frac{1}{2}\mu w$ which represents the contribution due to a uniform cylinder which extends from the propeller plane downstream to infinity. In the real case the wake boundary vortex system which is formed by the

vortex filaments shed at the shroud trailing edge and was replaced by the uniform cylinder must be continued within the shroud to where it is joined to the blade bound vortices at the blade tips as described in Appendix I. The assumed cylindrical wake boundary vortex system extension was considered to be a part of the shroud bound vortex system in section III-C-4 and hence its effect must be removed and the effect of the actual helical system must now be added. The induced velocity at the blade axis of this semi-infinite helical wake is approximately $\frac{1}{2} W \cos^2 \varphi_p$ and the tangential component is approximately $\frac{1}{2} W \sin \varphi_p \cos \varphi_p$ since the total induced velocity is nearly normal to the sheet.

B. From the curves of $K(x)$ versus $x$ for various numbers of blades and wake geometric pitches, the particular blade bound vortex strength may be found from

$$\Gamma(x) = \frac{2\pi (V_\infty + w) w}{b \Omega} K(x) \qquad (IV-17)$$

C. From the Kutta-Joukowski theorem

$$L' = \rho V \Gamma = \frac{1}{2} \rho V^2 c_\ell c \qquad (IV-18)$$

where $L'$ local lift per unit span

$c_\ell$ local section lift coefficient

$c$ local blade chord

At any particular blade section the total relative velocity $V$ is

$$V = \left\{ \left( \Omega r + \frac{1}{2} W \sin \varphi_p \cos \varphi_p \right)^2 + \left( V_\infty + \frac{1}{2} W \cos^2 \varphi_p + w_p - \frac{1}{2} x W \right)^2 \right\}^{\frac{1}{2}} \qquad (IV-19)$$

so that

$$\Gamma(x) = \tfrac{1}{2} c_l c V \qquad (IV-20)$$

Defining a solidity $\sigma$ where

$$\sigma = \frac{b c}{2 \pi r} \qquad (IV-21)$$

the following is obtained

$$\sigma c_l = \frac{2 W (V_\infty + w) K(x)}{\Omega r \left\{ \left(\Omega r + \tfrac{1}{2} w \sin\varphi_p \omega_2 \varphi_p\right)^2 + \left(V_\infty + \tfrac{1}{2} w \omega_2^2 \varphi_p + w_p - \tfrac{1}{2} u w\right)^2 \right\}^{1/2}} \qquad (IV-22)$$

D. For a given $c_l$ distribution across the blade span, calculate the chord distribution using the $\sigma c_l$ determined from equation IV-22. Then the choice of the $c_l$ and corresponding airfoil section is up to the designer, but in general, the $c_l$ should be the design $c_l$ of the section. Note also that strictly speaking, the chord line is a section of a helix and the thickness distribution should be laid out with respect to this helical line.

E. From the two-dimensional airfoil data for the sections chosen in D above plot the profile drag coefficient $c_d$ versus $x$. The contribution of the drag force to the thrust and power may be determined by graphical integration of the following integrals.

$$c_{s_d} = 2 \int_0^1 \frac{V(V_\infty + \tfrac{1}{2} w \omega_2^2 \varphi_p + w_p - \tfrac{1}{2} u w)}{V_\infty^2} \sigma c_d x \, dx \qquad (IV-23)$$

$$c_{p_d} = 2 \int_0^1 \frac{V(\Omega R)^2}{V_\infty^3} \sigma c_d x^3 \, dx \qquad (IV-24)$$

where $\kappa_{s_d}$ increment in thrust coefficient due to profile drag

$\kappa_{p_d}$ increment in power coefficient due to profile drag

and $V$ is determined from equation IV-19 .

VI. Propulsive Efficiency

A. An estimate of the shroud skin friction drag may be obtained by considering the velocity on the outer shroud contour to be free stream and that on the inner contour to be $V_\infty + w$ so that for an average skin friction drag coefficient $\kappa_{d_f}$

$$C_{D_s} = \kappa_{d_f} \frac{\frac{1}{2}\rho\left[V_\infty^2 S_o + (V_\infty + w)^2 S_i\right]}{\frac{1}{2}\rho V_\infty^2 F} \qquad (IV-25)$$

where $C_{D_s}$ shroud drag coefficient

$S_o$ outer wetted surface

$S_i$ inner wetted surface

B. The net thrust coefficient on the complete system is

$$\kappa_{s_T} = \kappa_s - \kappa_{s_d} - C_{D_s} \qquad (IV-26)$$

The power input is

$$\kappa_{p_T} = \kappa_p + \kappa_{p_d} + C_{D_s} \qquad (IV-27)$$

The propulsive efficiency is

$$\eta = \frac{\kappa_{s_T}}{\kappa_{p_T}} \qquad (IV-28)$$

It is to be noted that the total thrust coefficient includes that contributed by both the shroud and the propeller so that the integral of the axial component of the resultant force on the blade elements will not in general be equal to the total thrust less shroud skin friction drag as obtained in equation IV-26 .

## REFERENCES


1. Betz, A., Schrauben propeller mit geringstem Energieverlust. Göttinger Nochr, p. 193, 1919. (Screw Propeller with Minimum Energy Loss. National Research Council for Canada Technical Translation 736, 1958).

2. Goldstein, S., On the Vortex Theory of Screw Propellers. Proc. Roy. Soc. (London), ser. A., vol. 123, No. 792, pp. 440 - 465, April 5, 1929.

3. Theodorsen, T., Theory of Propellers, McGraw-Hill Book Co., Inc., New York, 1948. (Also available as NACA TR Nos. 775, 776, 777, and 778. 1944).

4. Malavard, L. C., The Use of Rheoelectric Analogies in Aerodynamics, AGARDograph 18, Aug. 1956.

5. Lamb, Horace, Hydrodynamics, Sixth edition, Dover Publications, New York, 1945.

6. Kuchemann, Dietrich and Weber, Johanna, Aerodynamics of Propulsion. First edition, McGraw-Hill Book Co., Inc., New York, 1953.

7. Abbott, Ira H., Fuselage-Drag Tests in the Variable-Density Tunnel: Streamline Bodies of Revolution, Fineness Ratio of 5. NACA TN 614, Sept., 1937.

DISTRIBUTION LIST

Final Report

"An Investigation of an Approach to the Problem
of Determining the Optimum Design of Shrouded Propellers"
Prepared under Contract DA 44-177-TC-402, Job Order Number 2

Chief of Transportation
Department of the Army
Washington 25, D. C.
ATTN: TCACR (2)
ATTN: TCRES (1)

Commanding General
U. S. Army Transportation Materiel Command
P. O. Box 209, Main Office
St. Louis 66, Missouri
ATTN: TCMC-APU (1)

Commanding Officer
U. S. Army Transportation Research Command
Fort Eustis, Virginia
ATTN: Research Reference Center (4)
ATTN: Aviation Directorate (6)

Chief of Naval Research
Code 461
Washington 25, D. C. (3)

Director of Defense Research and Engineering
Room 3E - 1065, The Pentagon
Washington 25, D. C.
ATTN: Technical Library (1)

U. S. Army Standardization Group, U. K.
Box 65, U. S. Navy 100
FPO New York, New York (1)

Librarian
Langley Research Center
National Aeronautics and Space Administration
Langley Field, Virginia (1)

Armed Services Technical Information Agency
Arlington Hall Station
Arlington 12, Virginia
ATTN: TIPCR (10)

Office of Chief of R&D
Department of the Army
Washington 25, D. C.
ATTN: Air Mobility Division

Office of the Senior Standardization Re
U. S. Army Standardization Group, Cana
c/o Director of Equipment Policy
Canadian Army Headquarters
Ottawa, Canada

Canadian Liaison Officer
U. S. Army Transportation School
Fort Eustis, Virginia

British Joint Services Mission (Army S
DAQMG (Mov & Tn)
1300 Massachusetts Avenue, N. W.
Washington 8, D. C.
ATTN: Lt. Col. R. J. Wade, RE

Office of Technical Services
Acquisition Section
Department of Commerce
Washington 25, D. C.

Mr. John J. Glennon, Librarian
Institute of the Aeronautical Sciences
2 E. 64th Street
New York 21, New York

Chief
U. S. Army R&D Liaison Group (9851 DU)
APO 757
New York, New York
ATTN: USATRECOM LO

Commanding Officer and Director
David Taylor Model Basin
Aerodynamics Laboratory Library
Washington 7, D. C.

Commanding Officer
U. S. Army Transportation Research Comm
Wright-Patterson Air Force Base, Ohio

Republic Aviation Corporation
Farmingdale, Long Island, New York
ATTN: Dr. Theodore Theodorsen

UNCLASSIFIED